

HFES: A HEIGHT FUNCTION METHOD WITH EXPLICIT INPUT AND SIGNED OUTPUT FOR HIGH-ORDER ESTIMATIONS OF CURVATURE AND UNIT VECTORS OF PLANAR CURVES*

QINGHAI ZHANG[†]

Abstract. The author proposes a height function (HF) method for estimating curvature and unit vectors of planar curves. The new method is named HFES since its signature consists of explicit input parameters (instead of implicit volume fractions) and signed output estimates. Due to this signature and its formal description, HFES has a number of appealing advantages. First, the convergence rate of HFES can be 4, 6, or a greater even integer. Second, local arcs can be rotated to further reduce leading truncation errors. Third, the sampling size of estimation is completely independent from the Eulerian grid size of the main flow. Fourth, signs of the signed output can be conveniently chosen by orientations of input Jordan curves, e.g., surface tension of a tracked material can be determined in a simple and worry-free manner. Last, HFES is applicable both to numerical simulation of multiphase flows and shape analysis in computer imaging. Furthermore, the author analyzes the effect of input perturbations upon output estimates, derives expressions of the best attainable accuracy afforded by a given input on uniform grids, and explains how to achieve this best accuracy with a concrete example. Results of numerical experiments with both exact and inexact input demonstrate that HFES can be much more accurate than previous HF methods. For the vortex-shear test of a circular disk, the eighth-order HFES coupled with the recent cubic iPAM method is millions of times more accurate than a fourth-order HF method coupled with volume-of-fluid methods! This drastic accuracy improvement is mainly due to the purely explicit spline representation of the curve and the rotation of local arcs.

Key words. height function, curvature estimation, surface tension, shape analysis, regular open sets, oriented Jordan curves

AMS subject classifications. 65D18, 65D25, 76T10

DOI. 10.1137/15M105001X

1. Introduction. Curvature measures how much a curve curves. As a fundamental concept of differential geometry, curvature plays an important role in an enormous range of scientific and engineering applications.

Computer imaging concerns the acquisition and processing of visual information via *planar shapes*, i.e., connected two-dimensional (2D) point sets [8]. The boundary of such a planar shape is often represented as a chain of corners where the curvature attains its zeros or extrema [15, 1, 16]. A classic example of the representational power of curvature is the drawing of a sleeping cat by Attneave [2, Figure 3], made from connecting 38 curvature extrema with straight lines. Apart from representing planar shapes, curvature is also very useful in identifying salient features for further transforming and classifying these shapes. It is therefore a task of essential importance to estimate curvature accurately.

Among the methods developed for curvature estimation in computer imaging, we mention three types: those based on the change in the slope angle of the tangent line [12, 3, 14], those based on derivatives of the curve [24, 23], and those based on

*Received by the editors November 30, 2015; accepted for publication (in revised form) January 4, 2017; published electronically April 25, 2017.

<http://www.siam.org/journals/sinum/55-2/M105001.html>

Funding: The work of the author was supported in part by the “One Thousand Youth Talents Plan” of China.

[†]School of Mathematical Sciences, Zhejiang University, Hangzhou, Zhejiang Province, 310027 China (qinghai@zju.edu.cn).

the radius of osculation circles [5, 6]. Before estimation, it is a common practice of this field to digitize a smooth input curve into a number of characteristic pixels and then connect them into a polygonal line to form the *approximate* input. This process of digitization incurs substantial approximation errors in the input polygon, which seriously limit the accuracy of curvature estimation in computer imaging [34, 17].

Another field that manifests the significance of curvature and unit vectors is the study of multiphase flows. As a ubiquitous example, the capillary effect on a phase interface is measured by the surface tension force, the magnitude of which is linearly proportional to that of the interface curvature. In numerically simulating interfacial flows, the lack of accuracy in curvature estimation leads to the well-known artifact of “parasitic currents” [18], which may induce strong spurious vortices and significantly destabilizes the tracked interface. To resolve this problem, many methods have been developed for accurate curvature estimation; some notable examples are the methods based on convolving the material color function with smooth kernels [33, 32], the PROST method based on quadratic polynomial fitting [28], and the height function (HF) method [13, 29]. Comparative studies [7, 9] show that the HF method can be superior to other methods in terms of accuracy.

In the HF method, information of an interface curve is *implicitly* captured by volume fractions of the material inside fixed control volumes (cells), with the volume fractions usually produced by an interface tracking method such as volume-of-fluid (VOF) methods. If no adaptive mesh refinement is employed, h_κ , the sampling size of estimation, equals h , the cell size for resolving the main flow.

The accuracy of HF methods may deteriorate when two interfaces get close and volume fractions of the tracked material do not faithfully reflect the information of either curve [7, 26]. For this scenario, improved HF methods [10, 22, 21] achieve better accuracy via modifying the volume fractions to be those from a single interface; see [22, Figure 2]. As another difficulty, the normal vector of the interface might have large alignment angle with grid lines, which may cause the height function to be ill-defined and results in large curvature estimation errors [22]. To alleviate this problem, several researchers [22, 20, 25] have explored the idea of rotating the local arc to better align its normal vector with grid lines. The successes, however, have been limited, probably because the explicit interface representation by piecewise linear interface reconstruction may be discontinuous across adjacent cells [25]. In addition, this idea has never been examined analytically.

All of the aforementioned methods are at best second-order accurate. Fourth- and higher-order HF methods are rare; we are aware of only those proposed by Sussman and Ohta [30, 31], Francois and Swartz [11], and Bornia et al. [4]. In addition, the application of which to nontrivial interface tracking problems is also rare; see [31], [39, section 6.3].

Previous HF methods only take volume fractions as their input. Then the targeting order-of-accuracy dictates that an estimated quantity correspond only to one particular point on the curve: the exact location of this point is calculated from abscissa of the grid lines that partition the domain; see [11] for such a formula. Consequently, estimated quantities for a cell may not even reside in that cell! For other estimation sites on the curve, one has to employ a certain interpolation procedure, which incurs a negative impact on the usefulness of the aforementioned fourth-order HF formulas because the codimension-1 nature of the curve limits the number of nearby intersections that are available for the fourth-order interpolation. See the ending paragraph of section 3 for more discussion.

Another relatively minor inconvenience of many current methods is the algorithmic ambiguity in terms of signs of their estimates. When needed, the sign is often determined in an ad hoc manner, and the implementation for a different application usually requires modifying the internal details of a program code; this is error-prone. In our opinion, it is the *signed* curvature and the *signed* normal vector that should be estimated, and an estimation algorithm should provide a clear and intuitive mechanism to let the user easily determine the sign from the physical context.

Even if the output estimates are signed, it may still be unclear how to determine the direction of surface tension force because this direction also depends on local shapes of the interface such as convexity and relative positions of the two materials. Therefore it would be very helpful to provide these two pieces of information.

The input curve in a real-world application always contains approximation errors. For computer imaging, Kovalevsky [17] showed that if the input curve is not exact, the curvature estimation error will be unbounded as the sampling size h_κ approaches zero. Furthermore, for a given inexact curve, errors of curvature estimation on uniform grids have a global minimum called the *best attainable accuracy*. Similar analysis for numerical simulations in multiphase flows would be very useful, but we are not aware of any.

So far we have discussed successes and limitations of previous curvature estimation methods in computer imaging and multiphase flow simulation. This work is motivated by questions relevant to both fields:

- (Q-1) Can we introduce a formal description of the HF methods so that fourth- and higher-order formulas may be systematically developed?
- (Q-2) Despite of the plethora of current methods, rigorous analysis on the accuracy of estimates is rare. Is it possible to formally prove the convergence rates?
- (Q-3) Given an input curve and its representation error, what is the expression of the best attainable accuracy on uniform grids? How do we achieve this best accuracy most efficiently?

In light of previous methods, we require that the proposed method

- (R-1) directly estimate the curvature and unit vectors for *any* point on the curve *without* interpolation,
- (R-2) completely decouple the sampling size h_κ from the Eulerian grid size h ,
- (R-3) provide via input parameters an intuitive and simple mechanism for the user to easily choose signs of the output,
- (R-4) reveal the local shape and relative positions of the two adjacent material regions so that surface tension forces can be *uniquely* determined.

Following our previous work on a generic framework [39] for analyzing interface tracking methods, we present a formal description of HF methods via a number of integral quantities that capture the local information of a curve. This answers (Q-1). By revisiting previous ideas such as rotating local arcs and including new elements such as splinegon clipping, we propose HFES, a family of new HF algorithms with explicit input parameters that meets all of the above requirements (R-1) to (R-4). The design of explicit input is discussed in section 3.1.

As an answer to (Q-2), a j th HFES algorithm is theoretically shown in section 4.1 to possess convergence rates of $2j$ in terms of the sampling size h_κ for $j = 1, 2, 3, 4$. The analysis also applies to most previous HF methods. In particular, we pinpoint in section 4.2 the reason why the rotation of local arcs leads to a better accuracy. Conceptually, the convergence rates of HFES can be any positive even integer $2j$ so long as a box of the size $(2j + 1)h_\kappa$ can still be considered as a local neighborhood of the estimation site p . The rest of section 4 contains an answer to (Q-3) via analysis.

In section 5, results of numerical experiments demonstrate the superior accuracy of HFES over that of previous HF methods and confirm the analysis in section 4. Also, the behavior of HFES is characterized by two nondimensional ratios in section 5.4, which leads to the observation in section 5.5.3 that curvature estimations in computer imaging and multiphase flows belong to two different asymptotic regimes. In section 5.5, we couple HFES to the recent (cubic) iPAM method [38, 39, 35] to establish that *the high-order accuracy of HFES can indeed be realized for practical interface tracking problems*. Furthermore, steps for efficiently extracting the best attainable accuracy from solutions of an interface tracking method are illustrated with a concrete example. Besides high-order HFES formulas and the explicit spline representation of the curve, the rotation of local arcs and the flexibility in selecting a sampling size $h_\kappa < h$ are shown in section 5.5.2 to be the other two main reasons for drastic accuracy improvements of HFES over previous HF methods.

We draw conclusions in section 6 with several research prospects.

2. Preliminaries and notation. In this section, we introduce notation and collect relevant concepts to form the theoretical ground of HFES. The definitions and conventions are carefully chosen so that they naturally lead to Proposition 2.2, the central result that addresses requirement (R-4) in section 1. While the last subsection is original, most contents in the other subsections can be found in a standard text on differential geometry such as [27].

2.1. A planar curve and the height function. An open *curve* is (the image of) a continuous map $\gamma : (\alpha, \beta) \rightarrow \mathbb{R}^n$ for some α, β with $-\infty \leq \alpha < \beta \leq +\infty$. It is *simple* if the map γ is injective. The *tangent vector of a curve* γ is its first derivative $\gamma' := \frac{d\gamma}{ds}$ and the *unit tangent vector* of γ , denoted by \mathbf{t} , is the normalization of its tangent vector. A *unit-speed curve* is a curve whose tangent vector has unit length at each of its points. A point $\gamma(t_0)$ is a *regular point* of γ if $\mathbf{t}(t_0)$ exists and $\mathbf{t}(t_0) \neq \mathbf{0}$ holds; a curve is *regular* if all of its points are regular. The *arc-length* of a curve starting at the point $\gamma(t_0)$, i.e., $s(t) = \int_{t_0}^t \|\gamma'(u)\|_2 du$, is a smooth function for a regular curve.

A map $X \mapsto Y$ is a *homeomorphism* if it is continuous and bijective and its inverse is continuous; then the two sets X and Y are said to be *homeomorphic*. A curve $\tilde{\gamma}(\tilde{\alpha}, \tilde{\beta}) \rightarrow \mathbb{R}^n$ is a *reparametrization* of another curve $\gamma(\alpha, \beta) \rightarrow \mathbb{R}^n$ if there exists a homeomorphism $\phi : (\tilde{\alpha}, \tilde{\beta}) \rightarrow (\alpha, \beta)$ such that $\tilde{\gamma}(\tilde{t}) = \gamma(\phi(\tilde{t}))$ for each $\tilde{t} \in (\tilde{\alpha}, \tilde{\beta})$. A reparametrization of a regular curve is unit-speed if and only if it is based on the arc-length.

By the implicit function theorem, a sufficiently small local arc of a planar curve $\tilde{\gamma}$ at a regular point p can always be reparametrized into the form

$$(2.1) \quad \gamma(\xi) = (\xi, H(\xi)),$$

where $H : \mathbb{R} \rightarrow \mathbb{R}$ is called the *height function* of γ associated with the parameter ξ and the axis ξ is either horizontal or vertical, i.e., $\xi = +x$, $\xi = -x$, $\xi = +y$, or $\xi = -y$.

2.2. Oriented Jordan curves. A *closed curve* is (the image of) a continuous map $\hat{\gamma} : [0, 1] \rightarrow \mathbb{R}^2$ that satisfies $\hat{\gamma}(0) = \hat{\gamma}(1)$. If the restriction of $\hat{\gamma}$ to $[0, 1)$ is further injective, then the closed curve is a *simple closed curve* or *Jordan curve*. The *Jordan curve theorem* states that the complement of a Jordan curve $\hat{\gamma}$ consists of two components: one is bounded and the other is unbounded; both of them are open and each has $\hat{\gamma}$ as its boundary.

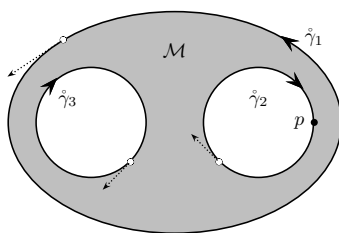


FIG. 1. Jordan curve representation of a physically meaningful region $\mathcal{M} \subset \mathbb{R}^2$ via orienting the Jordan curves that constitute its boundary. The shaded region represents \mathcal{M} , the solid lines the Jordan curves, the large arrows their orientations, and the dotted small arrows the induced tangent vectors at the boundary points. The outer Jordan curve is oriented positively and the inner Jordan curves negatively. As a consequence of these orientations, \mathcal{M} can be expressed as the intersection of interiors of these oriented Jordan curves, i.e., (2.2) holds with $n_{\mathcal{M}} = 3$.

The *interior* of a Jordan curve $\hat{\gamma}$, denoted by $\text{int}(\hat{\gamma})$, is the complement of $\hat{\gamma}$ that always lies to the left of an observer who traverses the curve in the increasing direction of its parameter; the other complement of $\hat{\gamma}$ is called the *exterior* of $\hat{\gamma}$. A Jordan curve $\hat{\gamma}$ is *positively oriented* if its interior is also its bounded complement. The *outward unit normal* \mathbf{n} of a Jordan curve $\hat{\gamma}$ is the unit normal vector that always points from its interior to its exterior.

A *splinegon* is the interior of an oriented simple closed spline.

2.3. Representing physically meaningful regions in the plane. As explained in the supplement to [39], regular open semianalytic sets are useful in modeling physically meaningful material regions as they are closed under Boolean operations and are free of low-dimensional features such as gaps or isolated vertices. In this work, a *Yin set* refers to a regular open semianalytic set $\mathcal{M} \subset \mathbb{R}^2$ with its boundary $\partial\mathcal{M}$ bounded. As shown in [37], a path-connected Yin set can be expressed as

$$(2.2) \quad \mathcal{M} = \text{int}(\hat{\gamma}_1) \cap \text{int}(\hat{\gamma}_2) \cap \cdots \cap \text{int}(\hat{\gamma}_{n_{\mathcal{M}}}),$$

where $\{\hat{\gamma}_i : i = 1, \dots, n_{\mathcal{M}}\}$ is a set of oriented pairwise disjoint Jordan curves. As illustrated in Figure 1, the representation is also unique up to the ordering of Jordan curves. This uniqueness is amenable to Proposition 2.2.

2.4. Signed unit normal and signed curvature. The *signed unit normal* of a curve, denoted by \mathbf{n}_s , is the unit vector obtained by rotating its unit tangent vector counterclockwise by $\frac{\pi}{2}$. The following proposition follows immediately from the above definitions.

PROPOSITION 2.1. *Let $\mathcal{M} \subset \mathbb{R}^2$ be a Yin set with its boundary Jordan curves oriented according to (2.2). Then the outward unit normal vector of \mathcal{M} is $\mathbf{n} = -\mathbf{n}_s$ at each regular point $p \in \partial\mathcal{M}$.*

For a unit-speed curve γ , its *signed curvature* is defined as

$$(2.3) \quad \kappa_s := \gamma'' \cdot \mathbf{n}_s.$$

The sign of κ_s indicates whether the unit tangent is locally rotating counterclockwise ($\kappa_s > 0$) or clockwise ($\kappa_s < 0$). For a regular local arc of the form (2.1), its signed curvature can be expressed as

$$(2.4) \quad \kappa_s = \frac{H''}{(1 + (H')^2)^{\frac{3}{2}}},$$

provided that the other local coordinate $\eta = H(\xi)$ is obtained by rotating the ξ -axis counterclockwise by $\frac{\pi}{2}$.

2.5. The sign of signed curvature and local convexity. A subset $\mathcal{M} \subseteq \mathbb{R}^2$ is *convex* if and only if for each pair of distinct points $p, q \in \mathcal{M}$ the line segment with endpoints p and q is contained in \mathcal{M} . Let $\mathcal{B}_r(p)$ denote the open ball centered at p with radius $r > 0$. A point set \mathcal{M} is said to be *locally convex at its boundary point* $p \in \partial\mathcal{M}$ if $\mathcal{B}_r(p) \cap \mathcal{M}$ is convex for a sufficiently small $r > 0$.

As a key to understand algorithms of the HFES method in section 3, the following proposition relates the Jordan curve representation of a physically meaningful area to local convexity in curvature estimation.

PROPOSITION 2.2. *Let $\mathcal{M} \subset \mathbb{R}^2$ be a Yin set with its boundary Jordan curves oriented according to (2.2). If $\kappa_s(p) > 0$ for some regular point $p \in \partial\mathcal{M}$, then \mathcal{M} is locally convex at p . If $\kappa_s(p) < 0$, then $\mathcal{M}^\perp := \mathbb{R}^2 \setminus (\mathcal{M} \cup \partial\mathcal{M})$ is locally convex at p .*

Proof. By (2.2), p must be on some Jordan curve $\hat{\gamma}_p \subseteq \partial\mathcal{M}$. Furthermore, by definition of the interior of a Jordan curve, \mathcal{M} must always lie on the left side of an observer who traverses $\hat{\gamma}_p$ according to its orientation.

Consider the case $\kappa_s(p) > 0$. Since the curvature of a smooth arc is a smooth function, we have $\kappa_s(q) > 0$ for all points $q \in \hat{\gamma}_p \cap \mathcal{B}_r(p)$ where $\mathcal{B}_r(p)$ is any open ball with sufficiently small radius r . Hence the tangent vector at each such q is rotating counterclockwise. Therefore $\mathcal{M}_p := \mathcal{M} \cap \mathcal{B}_r(p)$ lies entirely at the left side of the ray determined by any such q and its tangent vector.

Suppose \mathcal{M}_p is not convex. Then for some distinct pair of points $p_1, p_2 \in \mathcal{M}_p$ there exists an interval $[b_1, b_2] \subset (0, 1)$ such that $bp_1 + (1-b)p_2 \notin \mathcal{M}_p$ for all $b \in [b_1, b_2]$. On the other hand, $ap_1 + (1-a)p_2 \in \mathcal{B}_r(p)$ for all $a \in [0, 1]$ because $p_1, p_2 \in \mathcal{B}_r(p)$ and $\mathcal{B}_r(p)$ is convex. Hence $bp_1 + (1-b)p_2 \notin \mathcal{M}$ and the line segment with endpoints p_1 and p_2 must *properly* intersect $\hat{\gamma}_p \cap \mathcal{B}_r(p)$ at some point p_I . Consequently, p_1 and p_2 lie at different sides of the ray determined by p_I and its tangent vector, which contradicts the conclusion of the previous paragraph. Therefore, $\kappa_s(p) > 0$ implies that \mathcal{M} is locally convex at p .

Consider the case $\kappa_s(p) < 0$. Flipping orientations of all Jordan curves that constitute $\partial\mathcal{M}$ yields a new set of Jordan curves, which, by (2.2), represent \mathcal{M}^\perp . By (2.3) and the definition of signed unit normal, $\kappa_s(p) > 0$ for \mathcal{M}^\perp . Then the argument in previous paragraphs completes the proof. \square

3. Algorithms. After discussing the input design in section 3.1 and defining a number of auxiliary concepts in section 3.2, we answer (Q-1) by developing the HFESc and HFESv algorithms in sections 3.3 and 3.4 for respectively estimating curvature and unit vectors of a planar curve.

3.1. The HFES signature. When designing an algorithm, the input and output parameters as well as the preconditions and postconditions to be respectively imposed on them should be carefully chosen in order to maximize its application range and promote its reusability.

In previous HF methods, the input into curvature estimation is the set of volume fractions over fixed control volumes in the domain. For computer imaging, the input curve is usually an explicit representation of the curve such as a sequence of connected pixels. The input design of HFES is closer to the latter.

DEFINITION 3.1. *The HFES signature refers to the design that an HFES algorithm takes its input as the spline representation of an oriented piecewise smooth*

Jordan curve $\hat{\gamma}$, a sampling size h_κ , and a regular point $p \in \hat{\gamma}$ and outputs its estimates of the unit tangent vector \mathbf{t} , the signed unit normal vector \mathbf{n}_s , and the signed curvature κ_s of $\hat{\gamma}$ at the estimation site p .

This design choice comes from a number of considerations.

First, the inclusion of the estimation site p as an input parameter leads to the freedom of direct estimation at any point on the curve, meeting requirement (R-1).

Second, the fact that the sampling size h_κ is an independent input parameter furnishes a flexibility that meets requirement (R-2).

Third, representing the local arc at p by an explicit Jordan curve does not incur any loss of information, whereas that by implicit volume fractions do. It would be difficult to maintain high fidelity while rotating a local arc represented by volume fractions.

Fourth, the choice of a *single* Jordan curve precludes potential “contamination” of information that volume fractions may incur. Consider p in Figure 1. If the grid size of control volumes were not small enough, volume fractions of cells around p would contain information of not only $\hat{\gamma}_2$ but also $\hat{\gamma}_1$, hence the “contamination.” Clearly this will never happen with the input design in Definition 3.1.

Last, the orientation of the Jordan curve gives the user a simple mechanism with which to choose signs of the estimates, because flipping the orientation of the Jordan curve is equivalent to flipping signs of the signed output. This meets requirement (R-3). Furthermore, a single phase in multiphase flows can be represented by selecting the orientations of its boundary Jordan curves according to (2.2); then the local convexity of the phase at the estimation site can be automatically determined, as shown in Proposition 2.2. This appealing feature of HFES meets requirement (R-4).

Sometimes it is natural to have a simple open curve without orientation. Then the open curve needs to be closed into a Jordan curve, oriented in a way such that consequent signs of the estimates are appropriate for the problem at hand.

3.2. Discretely representing the local arc by a height function and volume fractions. Given the input $\hat{\gamma}$ and $p \in \hat{\gamma}$, we focus on a local arc $\gamma : (\alpha, \beta) \rightarrow \mathbb{R}^2$ that satisfies

$$(3.1) \quad \gamma \subset \hat{\gamma}, \quad \gamma(\xi) = (\xi, H(\xi)), \quad \gamma(0) = p, \quad |H'(0)| \leq 1,$$

where $\gamma(0) = p$ holds from a reparametrization of $\hat{\gamma}$ and the increasing direction of ξ in $\gamma(\xi) = (\xi, H(\xi))$ agrees with the orientation of $\hat{\gamma}$. As will be discussed in section 4, $|H'(0)| \leq 1$ is sufficient to guarantee numerical robustness. Figure 2 shows that $|H'(0)| \leq 1$ can always be fulfilled by a strategic choice of the local ξ -axis according to the tangent vector of γ at p .

We emphasize that the conditions in (3.1) are not assumptions that restrict the application range of HFES, but its *representation invariants* that facilitate algorithmic development and numerical analysis. The internal details of finding such an open curve γ are completely encapsulated inside HFES. In other words, the input into HFES needs to satisfy none of the conditions in (3.1).

As shown in Figure 2, we set up a local coordinate system (ξ, η) by first deducing the ξ -axis from the tangent vector of the arc γ and then rotate it counterclockwise by $\frac{\pi}{2}$ to obtain the η -axis. The neighborhood of p is then discretized by a rectangular mesh, of which the uniform grid size is the sampling size h_κ . Thus each cell \mathcal{C} is an open square and can be indexed by a multi-index $\mathbf{i} \in \mathbb{Z}^2$. For example, p is at the center of cell \mathcal{C}_0 , where $\mathbf{0}$ is the multi-index of which all components are zero. Two

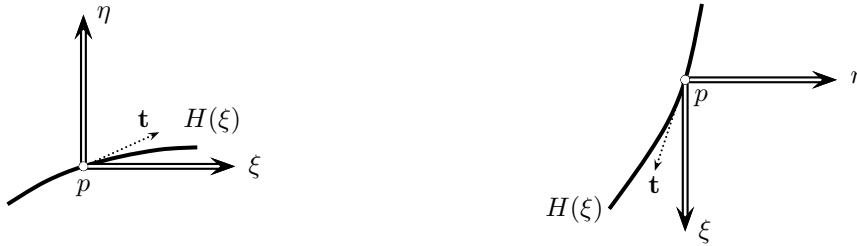
(a) a positive horizontal alignment: $\xi = x$ (b) a negative vertical alignment: $\xi = -y$

FIG. 2. The construction of local coordinates (ξ, η) to represent the local arc γ at p by a height function $\eta = H(\xi)$. An oriented Jordan curve $\hat{\gamma} \supset \gamma$ is given a priori and its orientation determines that of γ . A thick curve represents γ and a dotted arrow its unit tangent vector at p . The ξ -axis is chosen to align with one of the four directions, positive horizontal, negative horizontal, positive vertical, and negative vertical, so that the angle from \mathbf{t} to ξ is in the range $[-\frac{\pi}{4}, \frac{\pi}{4}]$. The η -axis is obtained by rotating the ξ -axis counterclockwise by $\frac{\pi}{2}$.

other multi-indices frequently used in this work are

$$(3.2) \quad \mathbf{e}^\xi := (1, 0), \quad \mathbf{e}^\eta := (0, 1).$$

DEFINITION 3.2 (sweeping parameters). For a regular point p on an open curve γ that satisfies (3.1), the j th sweeping interval is

$$(3.3) \quad I_j := \left(-j - \frac{1}{2}, j + \frac{1}{2}\right),$$

the j th local arc of γ is the restriction of γ to $h_\kappa I_j$,

$$(3.4) \quad \gamma_j := \{\gamma(\xi) : \xi \in h_\kappa I_j\},$$

the j th sweeping line segment is

$$(3.5) \quad S_j(v) := \{ah_\kappa \mathbf{e}^\xi + h_\kappa v \mathbf{e}^\eta : a \in I_j\},$$

and the j th sweeping range (v_j^-, v_j^+) is

$$(3.6) \quad \begin{cases} v_j^- := \max \{v \in \mathbb{Z}^- : S_j(v + \frac{1}{2}) \cap \gamma_j = \emptyset\} + \frac{1}{2}, \\ v_j^+ := \min \{v \in \mathbb{Z}^+ : S_j(v - \frac{1}{2}) \cap \gamma_j = \emptyset\} - \frac{1}{2}. \end{cases}$$

The above definition is illustrated in subplots (a) and (c) of Figure 3. For the j th sweeping range, j is analogous to the stencil width of previous HF methods while v_j^- and v_j^+ are analogous to a variable stencil height in [31] and [26, Figure 4]. For robustness, values of v_j^- and v_j^+ are determined within a box of finite size by moving the sweeping line one grid at a time until (3.6) is satisfied or until a boundary of the box is reached.

In addition to sweeping the neighborhood of p with a group of line segments, volume fractions defined for local cells also capture the information of the local arc.

DEFINITION 3.3 (h_κ -loop). For a regular point p on a curve γ satisfying (3.1), the j th h_κ -loop is a Jordan curve with positive orientation:

$$(3.7) \quad \hat{\gamma}_j := \mathbf{x}_1 \xrightarrow{\gamma_j} \mathbf{x}_2 \xrightarrow{\mathcal{L}(\mathbf{x}_2, \mathbf{x}_3)} \mathbf{x}_3 \xrightarrow{\mathcal{L}(\mathbf{x}_3, \mathbf{x}_4)} \mathbf{x}_4 \xrightarrow{\mathcal{L}(\mathbf{x}_4, \mathbf{x}_1)} \mathbf{x}_1,$$

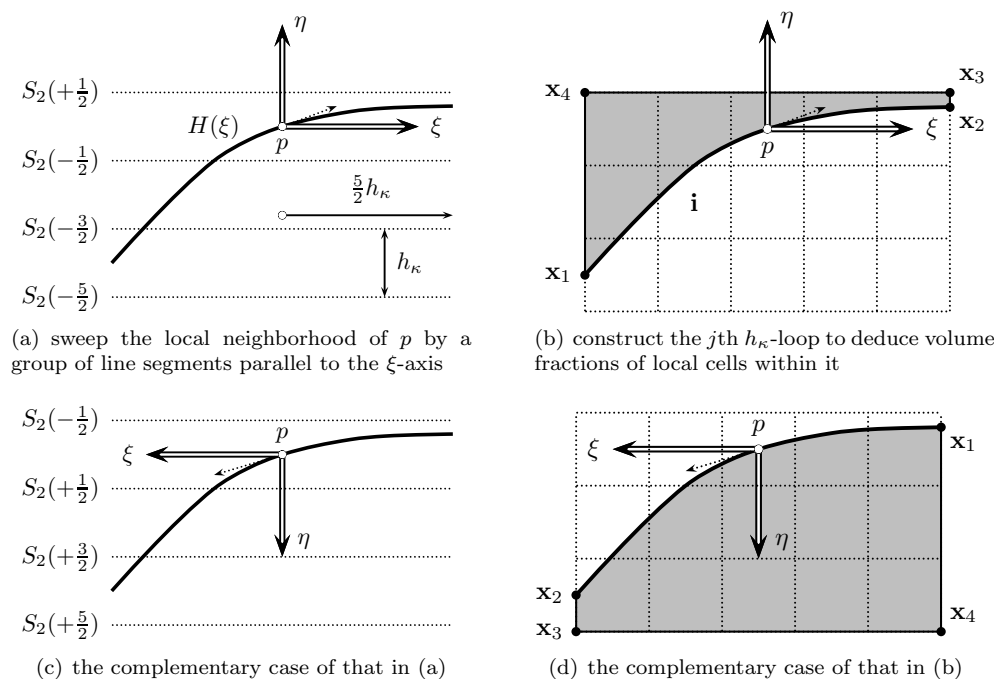


FIG. 3. Representing the local arc γ_j at p with a height function and volume fractions. A thick solid line is γ_j in (3.4) and a dotted arrow its unit tangent vector at p . In subplot (a), a dotted line is a sweeping line segment in (3.5) and γ_j is represented as the graph of a height function $H(\xi)$. According to (3.3) and (3.6), $j = 2$ and the sweeping range is $(v_2^-, v_2^+) = (-\frac{5}{2}, \frac{1}{2})$. In subplot (b), the shaded region is the interior of the h_κ -loop $\hat{\gamma}_j$ in (3.7), and the four vertices \mathbf{x}_1 , \mathbf{x}_2 , \mathbf{x}_3 , and \mathbf{x}_4 are as defined in (3.8). The cell with p at its center is indexed by $\mathbf{0}$ and any other cell is indexed by a linear combination of \mathbf{e}^ξ and \mathbf{e}^η in (3.2). In particular, $\mathbf{i} = -\mathbf{e}^\xi - \mathbf{e}^\eta$ and $\langle f \rangle_{\mathbf{i}} = \frac{1}{8}$. Subplots (c) and (d) illustrate the case complementary to that in subplots (a) and (b).

where γ_j is defined in (3.4), $\mathcal{L}(\mathbf{y}, \mathbf{z}) = \{a\mathbf{y} + (1-a)\mathbf{z} : a \in (0, 1)\}$ denotes the line segment connecting \mathbf{y} and \mathbf{z} , and the vertices are

$$(3.8) \quad \begin{cases} \mathbf{x}_1 := \gamma(-jh_\kappa - \frac{h_\kappa}{2}), \\ \mathbf{x}_2 := \gamma(jh_\kappa + \frac{h_\kappa}{2}), \\ \mathbf{x}_3 := (jh_\kappa + \frac{h_\kappa}{2}, v^+h_\kappa), \\ \mathbf{x}_4 := (-jh_\kappa - \frac{h_\kappa}{2}, v^+h_\kappa). \end{cases}$$

The simple-closedness of the h_κ -loop $\hat{\gamma}_j$ follows directly from (3.1) and Definitions 3.2 and 3.3. Then a *color function* can be defined from the interior of $\hat{\gamma}_j$ as

$$(3.9) \quad f(\mathbf{x}) := \begin{cases} 1, & \mathbf{x} \in \text{int}(\hat{\gamma}_j), \\ 0, & \mathbf{x} \notin \text{int}(\hat{\gamma}_j), \end{cases}$$

which naturally leads to the *volume fraction* of cell $\mathcal{C}_{\mathbf{i}}$,

$$(3.10) \quad \langle f \rangle_{\mathbf{i}} := \frac{1}{\|\mathcal{C}_{\mathbf{i}}\|} \int_{\mathcal{C}_{\mathbf{i}}} f(\mathbf{x}) \, d\mathbf{x} = \frac{\|\text{int}(\hat{\gamma}_j) \cap \mathcal{C}_{\mathbf{i}}\|}{h_\kappa^2},$$

where the *volume* of a regular open set $\mathcal{P} \subseteq \mathbb{R}^2$ with piecewise smooth boundary is $\|\mathcal{P}\| := \int_{\mathcal{P}} d\mathbf{x}$, and the piecewise smoothness of $\partial\mathcal{P}$ guarantees the existence of the

integral. Clearly, $\|\mathcal{C}_i\| = h_\kappa^2$ holds for all cells. The volume fractions induced by an h_κ -loop with $j = 2$ are illustrated in subplots (b) and (d) of Figure 3.

3.3. HFESv: Estimating unit vectors and curvature. The first step toward HFESv is to derive analytic expressions of unit vectors both in the local coordinates (ξ, η) and in the global coordinates (x, y) . It is not difficult to prove the following two propositions from definitions in the previous subsection.

PROPOSITION 3.4. *Consider a regular point p on an oriented Jordan curve $\hat{\gamma}$. Reparametrize the local arc γ at p so that (3.1) holds. Then, in the local coordinates (ξ, η) , the unit tangent and the outward unit normal of $\hat{\gamma}$ at p are given by*

$$(3.11a) \quad (t_\xi, t_\eta) = \frac{1}{\sqrt{\lambda_E}}(1, H'(0));$$

$$(3.11b) \quad (n_\xi, n_\eta) = \frac{1}{\sqrt{\lambda_E}}(H'(0), -1),$$

where $\lambda_E := 1 + (H'(0))^2$.

PROPOSITION 3.5. *Consider a regular point p on an oriented Jordan curve $\hat{\gamma}$. Reparametrize the local arc γ at p so that (3.1) holds. In the global coordinates (x, y) , the outward unit normal of $\hat{\gamma}$ at p is given by*

$$(3.12) \quad \mathbf{n} = \begin{cases} \frac{1}{\sqrt{\lambda_E}}(H'(0), -1) & \text{if } \xi \text{ is aligned with the positive } x\text{-axis,} \\ \frac{-1}{\sqrt{\lambda_E}}(H'(0), -1) & \text{if } \xi \text{ is aligned with the negative } x\text{-axis,} \\ \frac{1}{\sqrt{\lambda_E}}(-1, H'(0)) & \text{if } \xi \text{ is aligned with the positive } y\text{-axis,} \\ \frac{-1}{\sqrt{\lambda_E}}(-1, H'(0)) & \text{if } \xi \text{ is aligned with the negative } y\text{-axis,} \end{cases}$$

the signed unit normal by

$$(3.13) \quad \mathbf{n}_s = -\mathbf{n},$$

and the unit tangent vector by

$$(3.14) \quad \mathbf{t} = \begin{bmatrix} 0 & -1 \\ 1 & 0 \end{bmatrix} \mathbf{n}.$$

By (2.4) and Proposition 3.5, it suffices to numerically calculate $H'(0)$ and $H''(0)$. Thus the second step toward HFESv is to find expressions of $H'(0)$ and $H''(0)$ in terms of the volume fractions defined in (3.10).

DEFINITION 3.6 (averaged elevation). *For each $\ell = -j, \dots, -1, 0, 1, \dots, j$, the averaged elevation at column ℓ for the j th sweeping is*

$$(3.15) \quad \langle H \rangle_\ell := \frac{1}{h_\kappa^2} \int_{(\ell - \frac{1}{2})h_\kappa}^{(\ell + \frac{1}{2})h_\kappa} (H(\xi) - v_j^- h_\kappa) d\xi,$$

where v_j^- is the lower range of the j th sweeping in Definition 3.2.

DEFINITION 3.7 (column sum of volume fractions). *For the j th h_κ -loop, the ℓ th column sum of volume fractions is*

$$(3.16) \quad \langle F \rangle_\ell := \sum_{i_\eta \in (v_j^-, v_j^+)}^{i_\xi = \ell} \langle f \rangle_{\mathbf{i}},$$

where $\mathbf{i} = i_\xi \mathbf{e}^\xi + i_\eta \mathbf{e}^\eta$ is the index of a cell in the (ξ, η) coordinates.

As shown in Figure 2, the angle between ξ and the tangent vector of γ at p is no greater than $\frac{\pi}{4}$. Hence the direction of increasing ξ on the local arc γ_j agrees with the orientation of the h_κ -loop $\hat{\gamma}_j$. In Definition 3.3, $\hat{\gamma}_j$ is positive oriented, thus the bounded complement of $\hat{\gamma}$ lies at the left side of γ_j , and so do the points \mathbf{x}_3 and \mathbf{x}_4 . In comparison, (3.6) implies that the line segment $\{(\xi, v_j^-) : \xi \in I_j h_\kappa\}$ is at the right side of γ_j . Therefore, (3.10), (3.15), and (3.16) yield

$$(3.17) \quad \langle H \rangle_\ell + \langle F \rangle_\ell = v_j^+ - v_j^-.$$

DEFINITION 3.8 (approximating derivatives of height functions via column sums of volume fractions). *For a regular point p on a curve γ that satisfies (3.1), the j th symmetric approximation of the first two derivatives of the height function $H(\xi)$ is the inner products*

$$(3.18) \quad \begin{cases} \bar{H}'_j := -\mathbf{c}_{j,1} \cdot \hat{F}_j, \\ \bar{H}''_j := -\frac{1}{h_\kappa} \mathbf{c}_{j,2} \cdot \hat{F}_j, \end{cases}$$

where each component of the vector \hat{F}_j is a column sum of volume fractions in (3.16),

$$(3.19) \quad \hat{F}_j = \left(\langle F \rangle_{-j}, \dots, \langle F \rangle_{-1}, \langle F \rangle_0, \langle F \rangle_1, \dots, \langle F \rangle_j \right),$$

and the vectors of coefficients for $j = 1, 2, 3, 4$ are

$$(3.20) \quad \begin{aligned} \mathbf{c}_{1,1} &= \frac{1}{2}(-1, 0, 1), \\ \mathbf{c}_{1,2} &= (1, -2, 1), \\ \mathbf{c}_{2,1} &= \frac{1}{48}(5, -34, 0, 34, -5), \\ \mathbf{c}_{2,2} &= \frac{1}{8}(-1, 12, -22, 12, -1), \\ \mathbf{c}_{3,1} &= \frac{1}{11520}(-259, 2236, -9455, 0, 9455, -2236, 259), \\ \mathbf{c}_{3,2} &= \frac{1}{1920}(37, -462, 3435, -6020, 3435, -462, 37), \\ \mathbf{c}_{4,1} &= \frac{(3229, -33878, 170422, -574686, 0, 574686, -170422, 33878, -3229)}{645120}, \\ \mathbf{c}_{4,2} &= \frac{(-3229, 44480, -323260, 1912064, -3260110, 1912064, -323260, 44480, -3229)}{967680}. \end{aligned}$$

Note that the above formulas of $j = 1$ and $j = 2$ are essentially the same as those of the classical second-order HF method [13, 29] and the fourth-order HF method previously presented in [30, 4], respectively. The coefficients in (3.20) are generated by a MATLAB program that fits a local polynomial out of the cell averages of height functions. As shown in Figure 4, it is straightforward to derive coefficients of even higher-order approximations. For example, coefficients of the tenth-order formulas can be generated by simply setting the input `order` to 10.

It will be shown in Proposition 4.1 that \bar{H}'_j and \bar{H}''_j respectively approximate $H'(0)$ and $H''(0)$ to $(2j)$ th order accurate. However, the expressions of \bar{H}'_j and \bar{H}''_j in (3.18) depend on the alignment of ξ , which determines the cell indices of volume fractions in (3.19) and (3.16). Therefore the last step toward HFESv is to specify the alignment of ξ from the volume fractions.

Denote by $\mathbf{j} = j_x \mathbf{e}^x + j_y \mathbf{e}^y$ a cell index in the global coordinates (x, y) ; in particular, the cell $\mathbf{j} = \mathbf{0}$ has p at its center. The alignment of ξ is determined from the volume fractions as follows:

```

function [dH1, dH2] = deriveCurvatureFormulas(order)
syms h aHm5 aHm4 aHm3 aHm2 aHm1 aH0 aHp1 aHp2 aHp3 aHp4 aHp5;
tmp = [aHm5 aHm4 aHm3 aHm2 aHm1 aH0 aHp1 aHp2 aHp3 aHp4 aHp5];
shft = -order/2; nhl = (length(tmp)+1)/2;
cellAvgs = transpose(tmp(nhl+shft:nhl-shft));
A = sym(zeros(order+1, order+1));
for i=shft:1:order+shft % the polynomial is $\sum_{j=0}^{\text{order}}(a_j*x^j)$, the difference
    for j=0:1:order % of its integral at $(i\pm 0.5)h$ is the ith cell average
        A(i-shft+1, j+1) = ( (i+1/2)^(j+1)-(i-1/2)^(j+1) ) * h^j/(j+1);
    end
end
end
polyCoefs = A\cellAvgs;
for i=1:order+1
    dH1(i) = h*diff(polyCoefs(2), cellAvgs(i));
    dH2(i) = h*h*diff(2*polyCoefs(3), cellAvgs(i));
end

```

FIG. 4. The MATLAB program that generated the coefficients in (3.20).

(ALN-1) The local arc γ is said to be *horizontally aligned* if

$$(3.21) \quad \left| \sum_{j_y=-1,0,1}^{j_x=1} \langle f \rangle_{\mathbf{j}} - \sum_{j_y=-1,0,1}^{j_x=-1} \langle f \rangle_{\mathbf{j}} \right| < \left| \sum_{j_x=-1,0,1}^{j_y=1} \langle f \rangle_{\mathbf{j}} - \sum_{j_x=-1,0,1}^{j_y=-1} \langle f \rangle_{\mathbf{j}} \right|;$$

otherwise it is *vertically aligned*.

(ALN-2) If γ is horizontally aligned, further check whether the following holds:

$$(3.22) \quad \sum_{j_x=-1,0,1}^{j_y=1} \langle f \rangle_{\mathbf{j}} > \sum_{j_x=-1,0,1}^{j_y=-1} \langle f \rangle_{\mathbf{j}}.$$

The ξ -axis is determined to align with the positive x -axis if (3.22) holds; otherwise it aligns with the negative x -axis. These two cases are illustrated in subplots (b) and (d) of Figure 3, respectively.

(ALN-3) If γ is vertically aligned, further check whether the following holds:

$$(3.23) \quad \sum_{j_y=-1,0,1}^{j_x=1} \langle f \rangle_{\mathbf{j}} > \sum_{j_y=-1,0,1}^{j_x=-1} \langle f \rangle_{\mathbf{j}}.$$

The ξ -axis is determined to align with the negative y -axis if (3.23) holds; otherwise it aligns with the positive y -axis.

We are now ready to formally state HFESv, an algorithm for estimating the curvature and unit vectors of an oriented Jordan curve.

DEFINITION 3.9 (HFESv). *Given a sampling size h_κ and a regular point p on an oriented Jordan curve $\hat{\gamma}$, HFESv calculates the j th estimates ($j = 1, 2, 3, 4$) of the curvature and unit vectors at p as follows:*

- (HFESv-1) *Discretize the local neighborhood of p by square control volumes of size h_κ so that p is at the center of cell $\mathbf{0}$;*
- (HFESv-2) *Compute volume fractions $\langle f \rangle_{\mathbf{i}}$ as in (3.10) for each cell $\mathbf{i} \in [-i_{\max}, i_{\max}]^2$ with $i_{\max} = \max(j, |v_j^-|, v_j^+)$ by the splinegon clipping algorithm detailed in [35];*
- (HFESv-3) *Determine the alignment of ξ by the steps (ALN-1), (ALN-2), and (ALN-3)*

(HFESv-4) Calculate the j th symmetric approximations \bar{H}'_j and \bar{H}''_j by Definition 3.8;

(HFESv-5) Estimate the outward unit normal by \mathbf{n}_j , which is obtained from replacing $H'(0)$ and λ_E in (3.12) respectively with \bar{H}'_j and

$$(3.24) \quad \lambda_j := 1 + (\bar{H}'_j)^2;$$

(HFESv-6) Estimate the signed unit normal by $\mathbf{n}_{s,j} := -\mathbf{n}_j$ and the unit tangent by \mathbf{t}_j , which is obtained from replacing \mathbf{n} in (3.14) with \mathbf{n}_j ;

(HFESv-7) Estimate the signed curvature at p by

$$(3.25) \quad \kappa_j := \frac{1}{\sqrt{\lambda_j^3}} \bar{H}''_j.$$

The steps (HFESv-1) through (HFESv-5) form a standalone algorithm for estimating the outward unit normal. Also, (HFESv-3) through (HFESv-7) can be used as another standalone algorithm for curvature estimation if the input were volume fractions instead of an explicit curve. However, we are not advocating that volume fractions be used as the input into HFESv; see the discussions in the last paragraph of section 3.4 for two reasons. Instead, we are emphasizing that the analysis of HFES in section 4 also applies to previous HF methods that takes volume fractions as their input.

3.4. HFESc: Improving the estimation of curvature via rigid-body rotation. It follows from (3.25) and (3.24) that when $|\bar{H}'_j| \rightarrow 0$, the error of curvature estimation will be dominated by that of estimating $H''(0)$ with \bar{H}''_j . Hence a reduction of $|\bar{H}'_j|$ via a curvature-preserving transformation of the local arc is likely to improve the accuracy of curvature estimation. This observation leads to an improvement of HFESv via a rigid-body rotation of the local arc.

DEFINITION 3.10 (HFESc). Given a sampling size $h_\kappa > 0$ and a regular point p on an oriented Jordan curve $\hat{\gamma}$, HFESc calculates the j th estimate ($j = 1, 2, 3, 4$) of the curvature at p as follows:

(HFESc-1) Perform steps (HFESv-1) through (HFESv-5) in Definition 3.9 to obtain \mathbf{n}_j as the estimate of the outward unit normal;

(HFESc-2) Rotate the local arc around p as a rigid body such that the new outward unit normal at p is $(0, 1)$, i.e., along the positive y -axis;

(HFESc-3) Perform steps (HFESv-1) through (HFESv-7) to estimate the curvature at p .

The sole purpose of (HFESc-1) is to estimate the outward unit normal at p . In (HFESc-2), the local arc is rotated around p with its curvature preserved. In (HFESc-3), the HFESv algorithm is performed again to estimate the curvature with \bar{H}'_j close to zero. The key steps of HFESc are illustrated in Figure 5, where it is clear that magnitudes of v_j^- and v_j^+ in (HFESc-3) tend to be less than those in (HFESc-1).

A case study in section 4.2 shows that the curvature estimation error of HFESc can be much smaller than that of HFESv, which is confirmed by results of numerical experiments in section 5. For this reason, HFESv will be primarily used for estimating the unit vectors while HFESc is used only for estimating the curvature.

We have used a uniform grid size h_κ for curvature estimation in HFES algorithms. For nonuniform grids under the VOF+HF framework, the reader is referred to the analysis and formulas presented in [11]. Two crucial difference between HFES and

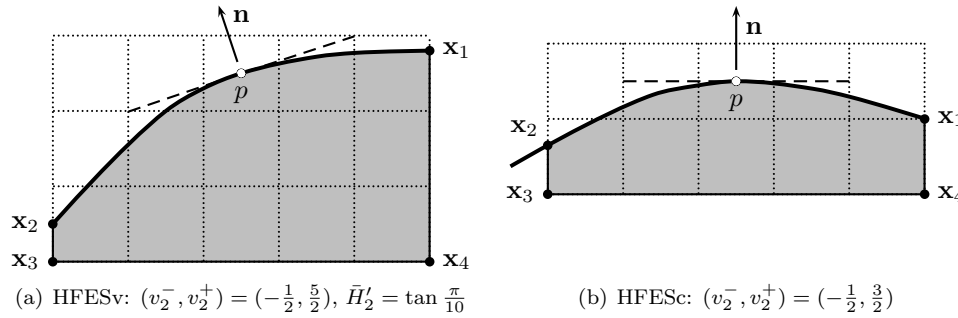


FIG. 5. Steps of curvature estimation in HFESc for the case shown in Figure 3(d). First, HFESv is used to estimate the outward unit normal \mathbf{n} . Then the local arc is rotated clockwise by $\frac{\pi}{10}$ so that the tangent line at p is horizontal. Last, HFESv is employed once again for a more accurate estimate of the curvature at p , as shown in subplot (b). In both subplots, \mathbf{x}_1 , \mathbf{x}_2 , \mathbf{x}_3 , and \mathbf{x}_4 represent vertices of the h_κ -loop and the light gray area its interior.

previous high-order HF methods [30, 31, 11, 4] are emphasized here. First, previous HF methods have the constraint that h_κ be no less than the Eulerian grid size h of the main flow. When nonuniform grids are adopted in resolving the main flow, one *has to* vary h_κ from cell to cell and hence the formulas presented in [11] are a *must*. In comparison, HFES algorithms meet requirement (R-2) posed in section 1 that h_κ be completely decoupled from h . Consequently, formulas for nonuniform grids are *never* needed in HFES. Second, previous HF methods take volume fractions as the input; thus only at a finite number of points can the curvature be estimated. As a result, one *has to* resort to interpolation for curvature estimation at other points; fourth- or higher-order accuracy is not always possible for all points on the curve because there might not exist enough estimated curvature for an accurate interpolation. In contrast, HFES algorithms take a given regular point p as an input parameter; the volume fractions specifically for p are then deduced from the explicit representation *inside* the algorithm. Hence, curvature can be estimated for any point on the curve without interpolation. This meets requirement (R-1) posed in section 1.

4. Analysis. In section 4.1, we answer question (Q-2) by proving that the j th HFES estimates are $(2j)$ th-order accurate when the input curve is exact. If the input curve contains approximation errors, it is argued in section 4.3 that the curvature estimation error will be unbounded as the sampling size h_κ approaches zero. Fortunately, there exists a critical sampling size $h_{c,j}^*$ such that its corresponding error $E_{c,j}^*$ is the best attainable accuracy. In section 4.4, we partially answer question (Q-3) by deriving expressions of $h_{c,j}^*$ and $E_{c,j}^*$ in terms of j , derivatives of the local height function, and the max-norm of representation error of the input curve.

4.1. The $(2j)$ th-order accuracy of the j th HFES estimates. HFESv is essentially obtained by approximating the first two derivatives of the height function. Naturally an accuracy analysis starts with the symmetric approximations.

PROPOSITION 4.1. *The j th symmetric approximations in Definition 3.8 are $(2j)$ th-order accurate, i.e.,*

$$(4.1) \quad \begin{cases} \bar{H}'_j = H'(0) + O(h_\kappa^{2j}), \\ \bar{H}''_j = H''(0) + O(h_\kappa^{2j}). \end{cases}$$

Proof. Construct a function

$$(4.2) \quad g(\xi) := \int_{-(j+1)h_\kappa}^{\xi} (H(z) - v_j^- h_\kappa) \, dz.$$

The first fundamental theorem of calculus yields

$$(4.3) \quad g'(\xi) = H(\xi).$$

It follows from (4.2) and (3.15) that

$$(4.4) \quad \langle H \rangle_\ell = \frac{1}{h_\kappa^2} g \left(\ell h_\kappa + \frac{h_\kappa}{2} \right) - \frac{1}{h_\kappa^2} g \left(\ell h_\kappa - \frac{h_\kappa}{2} \right).$$

For $j = 1$, we have

$$(4.5) \quad \begin{aligned} \bar{H}'_1 &= -\frac{1}{2} (\langle F \rangle_1 - \langle F \rangle_{-1}) = \frac{1}{2} (\langle H \rangle_1 - \langle H \rangle_{-1}) \\ &= \frac{1}{2h_\kappa^2} [g(\tfrac{3}{2}h_\kappa) + g(-\tfrac{3}{2}h_\kappa)] - \frac{1}{2h_\kappa^2} [g(\tfrac{1}{2}h_\kappa) + g(-\tfrac{1}{2}h_\kappa)] \\ &= \frac{1}{h_\kappa^2} [g(0) + \frac{9}{8}h_\kappa^2 g''(0) + \frac{81}{384}h_\kappa^4 g^{(4)}(0) + O(h_\kappa^6)] \\ &\quad - \frac{1}{h_\kappa^2} [g(0) + \frac{1}{8}h_\kappa^2 g''(0) + \frac{1}{384}h_\kappa^4 g^{(4)}(0) + O(h_\kappa^6)] \\ &= g''(0) + \frac{5}{24}g^{(4)}(0)h_\kappa^2 + O(h_\kappa^4) \\ &= H'(0) + \frac{5}{24}H^{(3)}(0)h_\kappa^2 + O(h_\kappa^4), \end{aligned}$$

where the first line follows from (3.18) and (3.17), the second line from (4.4), the third line from Taylor expansions of g at 0, and the last line from (4.3).

Similarly, the second identity in (4.1) can be proved for $j = 1$,

$$(4.6) \quad \begin{aligned} \bar{H}''_1 &= -\frac{1}{h_\kappa} (\langle F \rangle_1 - 2\langle F \rangle_0 + \langle F \rangle_{-1}) = \frac{1}{h_\kappa} (\langle H \rangle_1 - 2\langle H \rangle_0 + \langle H \rangle_{-1}) \\ &= \frac{1}{h_\kappa^3} [g(\tfrac{3}{2}h_\kappa) - g(-\tfrac{3}{2}h_\kappa) - 3g(\tfrac{1}{2}h_\kappa) + 3g(-\tfrac{1}{2}h_\kappa)] \\ &= \frac{2}{h_\kappa^3} [\tfrac{3}{2}h_\kappa g'(0) + \frac{27}{48}h_\kappa^3 g^{(3)}(0) + \frac{243}{3840}h_\kappa^5 g^{(5)}(0) + O(h_\kappa^7)] \\ &\quad - \frac{6}{h_\kappa^3} [\tfrac{1}{2}h_\kappa g'(0) + \frac{1}{48}h_\kappa^3 g^{(3)}(0) + \frac{1}{3840}h_\kappa^5 g^{(5)}(0) + O(h_\kappa^7)] \\ &= g^{(3)}(0) + \frac{1}{8}g^{(5)}(0)h_\kappa^2 + O(h_\kappa^4) \\ &= H''(0) + \frac{1}{8}H^{(4)}(0)h_\kappa^2 + O(h_\kappa^4). \end{aligned}$$

For $j = 2, 3, 4$, the identities in (4.1) can be proved by derivations similar to (4.5) and (4.6), although the algebra is more complex. \square

The representation invariant $|H'(0)| \leq 1$ in (3.1) and the expression of λ_E in Proposition 3.4 yield tight upper and lower bounds of λ_E , which, together with Proposition 4.1, further yield upper and lower bounds of λ_j ,

$$(4.7) \quad \begin{cases} \lambda_E \in [1, 2], \\ \lambda_j \in [1, 2] + O(h_\kappa^{2j}). \end{cases}$$

COROLLARY 4.2. *The j th HFESv estimate of unit vectors in Definition 3.9 are $(2j)$ th-order accurate, i.e.,*

$$(4.8) \quad \begin{cases} \mathbf{n}(0) = \mathbf{n}_j + O(h_\kappa^{2j}), \\ \mathbf{t}(0) = \mathbf{t}_j + O(h_\kappa^{2j}). \end{cases}$$

Proof. It suffices to only consider $\mathbf{n}(0) - \mathbf{n}_j$ for the case of ξ being aligned with the positive x axis. The definitions of λ_E and λ_j in Proposition 3.4 and Definition 3.9 yield

$$(4.9) \quad \begin{aligned} \frac{1}{\sqrt{\lambda_j}} - \frac{1}{\sqrt{\lambda_E}} &= \frac{\sqrt{\lambda_E} - \sqrt{\lambda_j}}{\sqrt{\lambda_j \lambda_E}} = \frac{\lambda_E - \lambda_j}{\sqrt{\lambda_j \lambda_E} (\sqrt{\lambda_j} + \sqrt{\lambda_E})} \\ &= \frac{(H'(0) - \bar{H}'_j)(H'(0) + \bar{H}'_j)}{\sqrt{\lambda_j \lambda_E} (\sqrt{\lambda_j} + \sqrt{\lambda_E})} \\ &= O(h_\kappa^{2j}), \end{aligned}$$

where the last line comes from $H'(0) - \bar{H}'_j = O(h_\kappa^{2j})$ in Proposition 4.1 and the fact that (4.7) and $|H'(0)| \leq 1$ imply $\frac{H'(0) + \bar{H}'_j}{\sqrt{\lambda_j \lambda_E} (\sqrt{\lambda_j} + \sqrt{\lambda_E})} = O(1)$. As for the other component,

$$\frac{\bar{H}'_j}{\sqrt{\lambda_j}} - \frac{H'(0)}{\sqrt{\lambda_E}} = \bar{H}'_j \left(\frac{1}{\sqrt{\lambda_j}} - \frac{1}{\sqrt{\lambda_E}} \right) + \frac{\bar{H}'_j - H'(0)}{\sqrt{\lambda_E}} = O(h_\kappa^{2j}),$$

where the last step follows from (4.9), (4.7), and Proposition 4.1. \square

From the above proof, the representation invariant $|H'(0)| \leq 1$ in (3.1) is sufficient to ensure numerical robustness by preventing the pathological cases of $H'(0) \rightarrow \pm\infty$, for which (4.8) might not hold.

PROPOSITION 4.3. *The j th HFESv and HFESc estimates of the signed curvature are $(2j)$ th-order accurate, i.e.,*

$$(4.10) \quad \kappa(0) = \kappa_j + O(h_\kappa^{2j}).$$

Proof. In light of (4.9), we have

$$(4.11) \quad \begin{aligned} \frac{1}{\sqrt{\lambda_E^3}} - \frac{1}{\sqrt{\lambda_j^3}} &= \frac{\sqrt{\lambda_E^3} - \sqrt{\lambda_j^3}}{\sqrt{\lambda_E^3 \lambda_j^3}} = \frac{\lambda_E^3 - \lambda_j^3}{\sqrt{\lambda_E^3 \lambda_j^3} (\sqrt{\lambda_E^3} + \sqrt{\lambda_j^3})} \\ &= K_\lambda (H'(0) - \bar{H}'_j)(H'(0) + \bar{H}'_j) \\ &= O(h_\kappa^{2j}), \end{aligned}$$

where

$$(4.12) \quad K_\lambda := \frac{\lambda_E^2 + \lambda_E \lambda_j + \lambda_j^2}{\sqrt{\lambda_E^3 \lambda_j^3} (\sqrt{\lambda_E^3} + \sqrt{\lambda_j^3})},$$

(4.7) implies $K_\lambda = O(1)$, and the last line of (4.11) follows from Proposition 4.1.

The distance between the exact and the approximated curvature is then

$$(4.13) \quad \begin{aligned} \left| \frac{H''(0)}{\sqrt{\lambda_E^3}} - \frac{\bar{H}''_j}{\sqrt{\lambda_j^3}} \right| &\leq |H''(0)| \left| \frac{1}{\sqrt{\lambda_E^3}} - \frac{1}{\sqrt{\lambda_j^3}} \right| + \frac{1}{\sqrt{\lambda_j^3}} |\bar{H}''_j - H''(0)| \\ &= O(h_\kappa^{2j}), \end{aligned}$$

where the first line follows from the triangle inequality and the second line from (4.11) and Proposition 4.1. \square

TABLE 1

Derivatives of the two height functions (4.15) and (4.16) that correspond to a circle with and without the rotation of local arcs, respectively. The radius and the angle are set to $R = 1$ and $\theta = \frac{\pi}{4}$. The fact of $H_c^{(i)} = 0$ for an odd $i > 1$ is due to the particularities of H_c and may not hold for other curves even when the rotation yields $H'_c = 0$. Note that $H'_c = 0$ only holds conceptually; in practice the rotation results in $\bar{H}'_c = 0$ and $H'_c = O(h_\kappa^{2j})$.

	$H_v^{(i)}(0)$	$H_c^{(i)}(0)$	$H_v^{(i)}(0)/H_c^{(i)}(0)$
$i = 1$	1	0	-
$i = 2$	2.83	1	2.83
$i = 3$	12	0	-
$i = 4$	1.02e+02	3	3.39e+01
$i = 5$	1.20e+03	0	-
$i = 6$	1.83e+04	45	4.07e+02
$i = 7$	3.43e+05	0	-
$i = 8$	7.58e+06	1.58e+03	4.82e+03
$i = 9$	1.94e+08	0	-
$i = 10$	5.61e+09	9.92e+04	5.66e+04

4.2. Accuracy improvement from rotation of local arcs: A simple case study. Rotation of local arcs yields $\bar{H}'_j = 0$ and Proposition 4.1 further implies $H'(0) = O(h_\kappa^{2j})$. Then for HFESc the estimate in (4.11) can be sharpened as

$$(4.14) \quad \frac{1}{\sqrt{\lambda_E^3}} - \frac{1}{\sqrt{\lambda_j^3}} = K_\lambda (H'(0) - \bar{H}'_j) (H'(0) + \bar{H}'_j) = O(h_\kappa^{4j}).$$

As another potential accuracy improvement, the error term $|\bar{H}''_j - H''(0)|$ in (4.13) for HFESc may be much smaller than that for HFESv, since the rotation of local arcs could change the form of the local height function. The rest of this subsection contains a simple case study to illustrate this point.

Consider a circle with radius R . For HFESc, the local neighborhood of any point p on the circle can be expressed as

$$(4.15) \quad \eta = H_c(\xi) = R - \sqrt{R^2 - \xi^2},$$

where (ξ, η) is the local coordinates with $\xi = 0$ at p . For HFESv, shift the global coordinates (x, y) so that their origin coincides with p and denote the center of the circle as $O = (x_0, y_0)^T$. Let $q = (x_0, y_0 - R)^T$ and denote by θ the angle from \vec{Oq} to \vec{Op} . For $\theta \in (0, \frac{\pi}{2})$, the local neighborhood of p on the circle can be expressed as

$$(4.16) \quad y = H_v(x) = R \cos \theta - \sqrt{R^2 - (x + R \sin \theta)^2}.$$

For $R = 1$ and $\theta = \frac{\pi}{4}$, the first to the tenth derivatives of the above two height functions are listed in Table 1, where $H_c^{(i)}(0)$ is much smaller than $H_v^{(i)}(0)$ for large i . By (4.6), we have $|\bar{H}''_j - H''(0)| = O(H^{(2j+2)} h_\kappa^{2j})$. Then Table 1 implies that $|\bar{H}''_j - H''(0)|$ of the eighth-order HFESc is over 50,000 times smaller than that of the eighth-order HFESv! Combining (4.13) and (4.6), we see clearly that HFESc can be much more accurate than HFESv.

4.3. Effects of input perturbations. In sections 4.1 and 4.2 the input curve into HFES is assumed to be exact; in reality, however, the input curve is seldom so. Even if an analytic expression of the curve is given, the discrete representation is

still of finite precision. Thus the effect of the input inexactness upon the estimation accuracy is an indispensable part of the numerical analysis.

Since the volume fractions in HFES algorithms are calculated from the approximate (or perturbed) curves, the errors in estimating derivatives of the height function should be defined accordingly as

$$(4.17) \quad E_{v,j} := \left| \tilde{H}'_j - H'(0) \right|, \quad E_{c,j} := \left| \tilde{H}''_j - H''(0) \right|,$$

where \tilde{H}'_j and \tilde{H}''_j are calculated by (3.18) from the perturbed height function \tilde{H} . The degree of perturbation/approximation is measured by a *perturbation length scale*

$$(4.18) \quad \epsilon_p := \max_{\xi} \left| H(\xi) - \tilde{H}(\xi) \right|.$$

If derivatives of the height function were estimated via finite-difference formulas, i.e., point values instead of averaged ones were used in Definitions 3.6, 3.7, and 3.8, the corresponding curvature estimation would have been much more sensitive to representation errors of the curve. Although the finite-difference schemes with spectral-like resolution [19] can achieve some damping effects of oscillations, they are limited to a finite range of frequencies and come at the price of lowering the order of accuracy. Note that the above discussion is not a criticism of the excellent work in [19], but merely a statement that formulas in [19], originally developed for simulating turbulence, are not suitable for curvature estimation in the current context.

In contrast, HFES estimates of unit vectors and curvature depend only on cell-averaged volume fractions. Due to the integral in (3.15), the final results are not sensitive to small-scale perturbations; see Figure 6 for an illustration. From the viewpoint of Fourier modes, the integral in (3.15) can be considered as a low-pass filter that damps high-frequency oscillations along the curve. Thus the finite-volume formulation furnishes an intrinsic insensitivity to small-scale perturbations and might be advantageous over methods based on finite differences. Finally, h_L , the length scale of numerical interface representation, is usually much smaller than h_κ in HFES, hence there could exist in the discrete interface abundant Fourier modes whose frequencies are higher than the highest one that can be resolved on a uniform grid of size h_κ . Therefore, the intrinsic damping of high-frequency modes is indeed of practical significance, and it is further demonstrated via numerical experiments in section 5.4.

In drastic comparison to the above insensitivity to small-scale perturbations is the adverse asymptotic behavior caused by approximating H with \tilde{H} ,

$$(4.19) \quad \epsilon_p \neq 0 \quad \Rightarrow \quad \lim_{h_\kappa \rightarrow 0} E_{c,j}(p) = +\infty,$$

which is due to Kovalevsky [17].

Taking $j = 1$, the triangle inequality and (4.6) yield

$$(4.20) \quad E_{c,1} \leq \left| \tilde{H}''_1 - H''(0) \right| + \left| \tilde{H}''_1 - \tilde{H}''_1 \right| \approx \frac{1}{8} H^{(4)}(0) h_\kappa^2 + \frac{4\epsilon_p}{h_\kappa^2} := E_{c,1}^{\max}(h_\kappa),$$

where the approximation mark “ \approx ” indicates that the higher-order truncation error $O(h_\kappa^4)$ in (4.6) has been dropped, and the coefficient 4 of ϵ_p comes from the 1-norm of $\mathbf{c}_{1,2}$ in (3.20) and accounts for the worst case of error accumulation. Since ϵ_p is a constant, the term $\frac{4\epsilon_p}{h_\kappa^2}$ in (4.20) is negligible when h_κ is sufficiently large.¹ However,

¹In particular, if the given problem is trivial in that $H^{(3)}(0) = 0$, one should choose h_κ to be sufficiently large to bound $|E_{c,j}|$ as a multiple of ϵ_p . In this work, we exclude this trivial case by assuming $H^{(i)}(0) \neq 0$ for each integer $i > 2$.

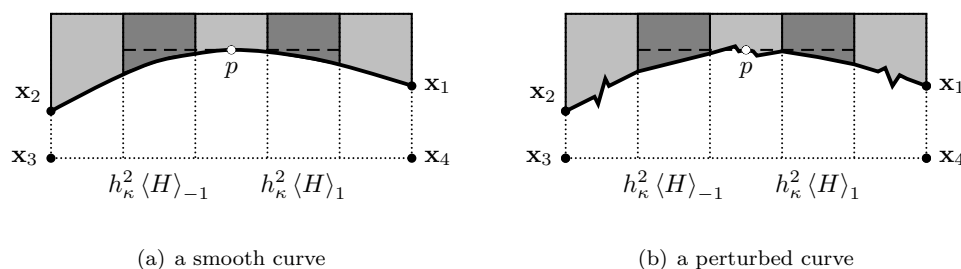


FIG. 6. The insensitivity of the HFES algorithms to small-scale perturbations. Subplots (a) and (b) show the case in Figure 5(b) without and with perturbations, respectively. For $j = 1$, the estimated unit vectors of the smooth curve and the perturbed curve are the same if they have the values of $h_\kappa^2 \langle H \rangle_{-1}$ and $h_\kappa^2 \langle H \rangle_1$, represented by the volumes of the dark gray regions in the two subplots. Similarly, for $j = 2$ the estimated curvatures of the two curves are the same if each of the five averaged elevations of the perturbed curve equals that of the smooth curve.

TABLE 2

Expressions of the best attainable accuracy and corresponding critical sampling sizes of HFES for estimating the first and second derivatives of the height function using (3.18). For accurate curvature estimation one should choose a sampling size h_κ that satisfies $h_\kappa > h_{c,j}^*$.

j	Order	$E_{c,j}^*$	$h_{c,j}^*$	$E_{v,j}^*$	$h_{v,j}^*$
1	2nd	$1.41\epsilon_p^{\frac{1}{2}} (H^{(4)})^{\frac{1}{2}}$	$2.38 \left(\frac{\epsilon_p}{H^{(4)}} \right)^{\frac{1}{4}}$	$1.12\epsilon_p^{\frac{2}{3}} (H^{(3)})^{\frac{1}{3}}$	$1.34 \left(\frac{\epsilon_p}{H^{(3)}} \right)^{\frac{1}{3}}$
2	4th	$1.67\epsilon_p^{\frac{2}{3}} (H^{(6)})^{\frac{1}{3}}$	$2.32 \left(\frac{\epsilon_p}{H^{(6)}} \right)^{\frac{1}{6}}$	$1.31\epsilon_p^{\frac{4}{5}} (H^{(5)})^{\frac{1}{5}}$	$1.55 \left(\frac{\epsilon_p}{H^{(5)}} \right)^{\frac{1}{5}}$
3	6th	$1.86\epsilon_p^{\frac{3}{4}} (H^{(8)})^{\frac{1}{4}}$	$2.28 \left(\frac{\epsilon_p}{H^{(8)}} \right)^{\frac{1}{8}}$	$1.46\epsilon_p^{\frac{6}{7}} (H^{(7)})^{\frac{1}{7}}$	$1.66 \left(\frac{\epsilon_p}{H^{(7)}} \right)^{\frac{1}{7}}$
4	8th	$2.01\epsilon_p^{\frac{4}{5}} (H^{(10)})^{\frac{1}{5}}$	$2.25 \left(\frac{\epsilon_p}{H^{(10)}} \right)^{\frac{1}{10}}$	$1.58\epsilon_p^{\frac{8}{9}} (H^{(9)})^{\frac{1}{9}}$	$1.72 \left(\frac{\epsilon_p}{H^{(9)}} \right)^{\frac{1}{9}}$

as h_κ is decreased, $\frac{4\epsilon_p}{h_\kappa^2}$ increases. In the asymptotic case of $h_\kappa \rightarrow 0$, the HFES estimations are meaningless since $E_{c,j} \rightarrow +\infty$.

4.4. The critical sampling size and the best attainable accuracy on uniform grids. For a fixed j , discussions in the previous subsection imply the existence of a critical sampling size $h_{c,j}^*$ for the nontrivial case of $H^{(2j+1)}(0) \neq 0$ such that, for all $h_\kappa > h_{c,j}^*$, a smaller value of h_κ implies a smaller value of $E_{c,j}$. For $j = 1$, this critical value is readily given by

$$(4.21) \quad \frac{\partial E_{c,1}^{\max}}{\partial h_\kappa} = 0 \Rightarrow h_{c,1}^* = \left(\frac{32\epsilon_p}{H^{(4)}(0)} \right)^{\frac{1}{4}};$$

clearly, only those sampling sizes satisfying $h_\kappa > h_{c,1}^*$ are appropriate. The error $E_{c,1}^*$ corresponding to $h_{c,1}^*$ is then the best attainable accuracy:

$$(4.22) \quad E_{c,1}^* := E_{c,1}^{\max}(h_{c,1}^*) = \left(2\epsilon_p H^{(4)}(0) \right)^{\frac{1}{2}}.$$

The above arguments can be repeated for $E_{v,1}$ and $j = 2, 3, 4$. In Table 2, we list the critical sampling sizes and the best attainable accuracy for estimating the first and second derivatives of the height function. Expressions of the best attainable

accuracy are all of the form

$$(4.23) \quad E_{c,j}^* = a_c^E \epsilon_p^{\frac{j}{j+1}} \left(H^{(2j+2)} \right)^{\frac{1}{j+1}}, \quad E_{v,j}^* = a_v^E \epsilon_p^{\frac{2j}{2j+1}} \left(H^{(2j+1)} \right)^{\frac{1}{2j+1}},$$

where the exponents of ϵ_p get closer to 1 as j increases. Note that the coefficients a_c^E and a_v^E grow slowly as j increases. In comparison, the corresponding critical sampling sizes are all of the form

$$(4.24) \quad h_{c,j}^* = a_c^h \epsilon_p^{\frac{1}{2j+2}} \left(H^{(2j+2)} \right)^{-\frac{1}{2j+2}}, \quad h_{v,j}^* = a_v^h \epsilon_p^{\frac{1}{2j+1}} \left(H^{(2j+1)} \right)^{-\frac{1}{2j+1}},$$

where exponents of ϵ_p get closer to 0 as j increases. The coefficients a_c^h and a_v^h change slowly as j increases.

We emphasize in passing that this so-called best attainable accuracy is limited to using *uniform* grids to capture the local information of the curve; there might as well exist a better accuracy of curvature estimation when nonuniform grids are employed at the local neighborhood of the estimation site.

5. Tests. After defining error criteria in section 5.1, we perform numerical tests in sections 5.2 and 5.3 to demonstrate the superior accuracy of HFES over those of previous HF methods. The effect of the input perturbation upon the best attainable accuracy is numerically investigated in section 5.4. In section 5.5, we couple HFES to the cubic iPAM method to demonstrate that the high accuracy of HFES can indeed be realized for practical interface motion problems. We also illustrate how to most efficiently achieve the best estimation accuracy from results of interface tracking methods.

5.1. Error criteria. In this work, the error in estimating the unit normal vector is based on the length of the error vector $\tilde{\mathbf{n}} - \mathbf{n}$, where \mathbf{n} is the exact unit normal vector and $\tilde{\mathbf{n}}$ the estimated unit normal vector:

$$(5.1) \quad E_{\mathbf{n}}(\tilde{\mathbf{n}}) := \|\tilde{\mathbf{n}} - \mathbf{n}\|_2.$$

Since both \mathbf{n} and $\tilde{\mathbf{n}}$ have unit length, the error in estimating the unit normal vector can also be measured by the angle θ between them. Two criteria frequently used in the literature are

$$(5.2) \quad E_{\mathbf{n}1}(\tilde{\mathbf{n}}) := \|\tilde{\mathbf{n}} - (\tilde{\mathbf{n}} \cdot \mathbf{n})\mathbf{n}\|_2;$$

$$(5.3) \quad E_{\mathbf{n}2}(\tilde{\mathbf{n}}) := 1 - \mathbf{n} \cdot \tilde{\mathbf{n}}.$$

Unfortunately, $E_{\mathbf{n}2}(\tilde{\mathbf{n}})$ in (5.3) is not appropriate since $\|\mathbf{n}\| = \|\tilde{\mathbf{n}}\| = 1$ leads to

$$(5.4) \quad 1 - \mathbf{n} \cdot \tilde{\mathbf{n}} = 1 - \frac{\mathbf{n} \cdot \tilde{\mathbf{n}}}{\|\mathbf{n}\| \|\tilde{\mathbf{n}}\|} = 1 - \cos \theta \approx \frac{\theta^2}{2}.$$

In other words, $E_{\mathbf{n}2}(\tilde{\mathbf{n}})$ misjudges a q th-order algorithm as $(2q)$ th-order accurate. As for $E_{\mathbf{n}1}(\tilde{\mathbf{n}})$ in (5.2), it is equivalent to $E_{\mathbf{n}}(\tilde{\mathbf{n}})$ in the asymptotic case of $\theta \rightarrow 0$ because (5.4) implies $\mathbf{n} \cdot \tilde{\mathbf{n}} \rightarrow 1$. In fact, $E_{\mathbf{n}1}(\tilde{\mathbf{n}})$ can be interpreted as the angle between the two unit normal vectors:

$$\|\tilde{\mathbf{n}} - (\tilde{\mathbf{n}} \cdot \mathbf{n})\mathbf{n}\|_2 = \frac{\|\tilde{\mathbf{n}} - (\tilde{\mathbf{n}} \cdot \mathbf{n})\mathbf{n}\|_2}{\|\tilde{\mathbf{n}}\|} = \sin \theta \rightarrow \theta,$$

where $(\tilde{\mathbf{n}} \cdot \mathbf{n})\mathbf{n}$ is the projection of $\tilde{\mathbf{n}}$ onto \mathbf{n} .

We prefer (5.1) over (5.2) for several reasons. First, (5.1) is easier and faster to compute than (5.2). Second, if $\tilde{\mathbf{n}} = -\mathbf{n}$, then $E_{\mathbf{n}}(\tilde{\mathbf{n}}) = 2$ while $E_{\mathbf{n}1}(\tilde{\mathbf{n}}) = 0$. Thus (5.1) is more precise in that it does not tolerate the incorrect sign of estimated unit normal vectors. Last, $E_{\mathbf{n}}(\tilde{\mathbf{n}})$ is more general: it does not depend on the algorithm detail $\|\tilde{\mathbf{n}}\| = 1$ while $E_{\mathbf{n}1}(\tilde{\mathbf{n}})$ does.

The computed unit normal and tangent vectors by HFES are always perpendicular, i.e., their inner product is zero up to machine precision. Therefore, it suffices to only report errors and convergence rates for estimating unit normal vectors, as those of the unit tangent vectors are exactly the same.

The accuracy of curvature estimation is measured by

$$(5.5) \quad E_{\kappa,j}(p) := \kappa_j - \kappa(p),$$

where both the exact curvature $\kappa(p)$ and the j th estimate κ_j are *signed* numbers.

In the numerical tests, each of the errors (5.1) and (5.5) is evaluated at multiple locations to obtain a vector \mathbf{E} . The convergence rates are then calculated based on the max-norm and q -norm as follows:

$$(5.6) \quad \mathcal{L}_{\infty}(\mathbf{E}(N)) = \|\mathbf{E}(N)\|_{\infty}, \quad \mathcal{L}_q(\mathbf{E}(N)) = \frac{1}{N^{1/q}} \|\mathbf{E}(N)\|_q,$$

where $q \in \mathbb{N}^+$ and N is the number of estimation sites.

5.2. A unit circle. In this test, the curvature and unit vectors at $\frac{2}{h_{\kappa}} - 1$ evenly spaced points² on the circumference of a unit circle are estimated for $h_{\kappa} = \frac{1}{16}, \frac{1}{32}, \frac{1}{64}$. Errors and convergence rates of HFES based on the max-norm and the 1-norm, together with those of previous HF methods, are listed in Tables 3 and 4.

Results in Tables 3 and 4 demonstrate the $(2j)$ th-order accuracy of the j th HFES estimates of curvature and unit vectors, which confirms Proposition 4.3 and Corollary 4.2. For the sixth- and eighth-order HFESc algorithms, several convergence-rate reductions are observed on the finest two grids in Table 3: the convergence rate based on the max-norm is 4.76 for the sixth-order HFESc and the accuracy of the eighth-order HFESc remains roughly the same. These reductions are not caused by the representation error of the circle since a further increase of the number of spline knots does not improve the accuracy. Instead, as discussed in section 4.4, nondecreasing or even increasing errors upon refining the grid indicate that the best attainable accuracy is nearby or has already been achieved.

Table 3 shows that HFESc is more accurate than HFESv in curvature estimation. For a fixed sampling size, the improvement ratio of HFESc over HFESv appears to increase as the order of accuracy increases. In particular, the eighth-order HFESc is thousands of times more accurate than the eighth-order HFESv in the max-norm error on the coarsest grid. These observations confirm the findings in section 4.2.

Curvature results of high-order HFESc algorithms can be much more accurate than those of an HF method. For $h_{\kappa} = \frac{1}{32}$, the improvement ratio of the eighth-order HFESc over the classical second-order HF method [13, 29] is over 20 million! This dramatic accuracy improvement is caused not only by the much smaller leading truncation error of the eighth-order HFESc than that of the second-order HF method, but also by the rotation of local arcs. Take the max-norm errors for $h_{\kappa} = \frac{1}{32}$. The improvement ratio of HFESv ($j = 4$) over the HF method is $2.40 \times 10^{-3} / 5.61 \times 10^{-7} \approx$

²The number " $\frac{2}{h_{\kappa}} - 1$ " has been deliberately chosen to avoid axisymmetry of these estimation sites on the circumference of the circle.

TABLE 3

Curvature error norms and convergence rates for the unit circle test. The sampling size of HFES is the same as the Eulerian grid size of previous HF methods. The unit circle is represented by cubic splines, for which the maximum distance between two adjacent knots is $0.5h_\kappa$, $0.1h_\kappa$, $0.02h_\kappa$, and $0.01h_\kappa$ for $j = 1, 2, 3, 4$, respectively.

Method	$\mathcal{L}_\infty(h_\kappa = \frac{1}{16})$	Rate	$\mathcal{L}_\infty(h_\kappa = \frac{1}{32})$	Rate	$\mathcal{L}_\infty(h_\kappa = \frac{1}{64})$
HFESv, $j = 1$	2.86e-03	1.99	7.20e-04	1.99	1.81e-04
HFESv, $j = 2$	6.67e-04	4.08	3.96e-05	3.98	2.51e-06
HFESv, $j = 3$	2.97e-04	6.44	3.43e-06	6.03	5.25e-08
HFESv, $j = 4$	3.28e-04	9.19	5.61e-07	8.17	1.95e-09
HFESc, $j = 1$	1.47e-03	2.00	3.67e-04	2.00	9.16e-05
HFESc, $j = 2$	1.35e-05	4.02	8.30e-07	4.00	5.18e-08
HFESc, $j = 3$	3.28e-07	6.04	4.97e-09	4.76	1.84e-10
HFESc, $j = 4$	1.59e-08	7.19	1.09e-10	-0.16	1.22e-10
HF [29]	1.04e-02	2.12	2.40e-03	2.00	6.00e-04
Method	$\mathcal{L}_1(h_\kappa = \frac{1}{16})$	Rate	$\mathcal{L}_1(h_\kappa = \frac{1}{32})$	Rate	$\mathcal{L}_1(h_\kappa = \frac{1}{64})$
HFESv, $j = 1$	1.22e-03	1.99	3.07e-04	1.99	7.72e-05
HFESv, $j = 2$	8.35e-05	4.13	4.76e-06	4.02	2.93e-07
HFESv, $j = 3$	2.36e-05	6.52	2.57e-07	6.10	3.76e-09
HFESv, $j = 4$	2.03e-05	9.34	3.14e-08	7.65	1.56e-10
HFESc, $j = 1$	9.49e-04	1.98	2.41e-04	1.99	6.06e-05
HFESc, $j = 2$	8.69e-06	3.99	5.45e-07	3.99	3.42e-08
HFESc, $j = 3$	2.12e-07	6.03	3.25e-09	5.96	5.20e-11
HFESc, $j = 4$	1.03e-08	8.05	3.87e-11	3.21	4.19e-12
HF [29]	3.70e-03	2.04	9.00e-04	2.17	2.00e-04

TABLE 4

Errors and convergence rates of unit vectors for the unit circle test. For caption see Table 3.

Method	$\mathcal{L}_\infty(h_\kappa = \frac{1}{16})$	Rate	$\mathcal{L}_\infty(h_\kappa = \frac{1}{32})$	Rate	$\mathcal{L}_\infty(h_\kappa = \frac{1}{64})$
HFESv, $j = 1$	4.52e-03	1.95	1.17e-03	1.97	2.98e-04
HFESv, $j = 2$	3.89e-04	4.02	2.40e-05	3.97	1.54e-06
HFESv, $j = 3$	1.25e-04	6.35	1.53e-06	6.01	2.37e-08
HFESv, $j = 4$	1.23e-04	9.17	2.13e-07	8.15	7.50e-10
HF [10]	2.86e-02	0.62	1.86e-02	1.00	9.27e-03
HF2 [10]	4.05e-03	2.06	9.70e-04	2.09	2.28e-04
Method	$\mathcal{L}_1(h_\kappa = \frac{1}{16})$	Rate	$\mathcal{L}_1(h_\kappa = \frac{1}{32})$	Rate	$\mathcal{L}_1(h_\kappa = \frac{1}{64})$
HFESv, $j = 1$	1.02e-03	1.99	2.56e-04	1.99	6.43e-05
HFESv, $j = 2$	4.86e-05	4.09	2.85e-06	4.02	1.76e-07
HFESv, $j = 3$	1.03e-05	6.44	1.19e-07	6.09	1.74e-09
HFESv, $j = 4$	7.62e-06	9.27	1.23e-08	8.24	4.08e-11
HF [10]	7.61e-03	1.60	2.51e-03	0.85	1.39e-03
HF2 [10]	1.17e-03	1.99	2.94e-04	2.02	7.26e-05

4278, whereas that of HFESc ($j = 4$) over HFESv ($j = 4$) is $5.61 \times 10^{-7} / 1.90 \times 10^{-10} \approx 5147$. Hence the accuracy improvement contributed by the rotation of local arcs can be greater than that by a high-order formula.

For these tests we also recorded the total CPU time consumed by the eighth-order HFESc and the HF method [29], with the latter method implemented by US in MATLAB. Note that the time for calculating the volume fractions is excluded from the timing results of the HF method. For all three grids, the CPU-time ratio of the eighth-order HFESc to the HF method is about 16, which is not surprising since for the former method about 90% of the total CPU time is spent on rotating the local arc and generating volume fractions from the explicit representation. Nonetheless, the expense of the eighth-order HFESc is acceptable because it could be millions of

TABLE 5

Curvature error norms and convergence rates for a cosine wave test. The sampling size of HFES is the same as the Eulerian grid size of previous HF methods. The cosine wave has the same form ($A = 3, B = -1, n = 4, L = 8$) as that in [7, 21] and is represented by cubic splines, for which the maximum distance between two adjacent knots is $0.5h_\kappa$, $0.1h_\kappa$, $0.02h_\kappa$, and $0.01h_\kappa$ for $j = 1, 2, 3, 4$, respectively. For HFESc, the curvature of the cosine wave is estimated at $\frac{10}{h_\kappa}$ points, the x -coordinates of which are evenly spaced between $x = 2$ and $x = 6$. Results of the improved HF method on the two coarse grids are taken from [21, Table 2], while those on the finest grid are obtained by extrapolation with the assumption that convergence rates are the same for all three grids. Convergence rates of the improved HF method are obtained from a constant number of 100 random points for all grids, while those of HFESc are obtained from 200, 400, and 800 evenly spaced points.

Method	$\mathcal{L}_\infty(h_\kappa = \frac{1}{20})$	Rate	$\mathcal{L}_\infty(h_\kappa = \frac{1}{40})$	Rate	$\mathcal{L}_\infty(h_\kappa = \frac{1}{80})$
HFESc, $j = 1$	4.50e-01	2.08	1.06e-01	2.02	2.62e-02
HFESc, $j = 2$	3.26e-01	5.05	9.82e-03	4.17	5.45e-04
HFESc, $j = 3$	7.92e-01	7.45	4.53e-03	7.19	3.11e-05
HFESc, $j = 4$	2.26e+00	9.29	3.62e-03	9.95	3.66e-06
Improved HF [21]	8.83e-01	2.80	1.30e-01	2.80	1.87e-02
Method	$\mathcal{L}_1(h_\kappa = \frac{1}{20})$	Rate	$\mathcal{L}_1(h_\kappa = \frac{1}{40})$	Rate	$\mathcal{L}_1(h_\kappa = \frac{1}{80})$
HFESc, $j = 1$	9.13e-02	2.06	2.18e-02	2.01	5.41e-03
HFESc, $j = 2$	4.57e-02	4.86	1.58e-03	4.15	8.90e-05
HFESc, $j = 3$	1.02e-01	7.79	4.62e-04	6.74	4.31e-06
HFESc, $j = 4$	2.32e-01	9.42	3.39e-04	9.57	4.47e-07
Improved HF [21]	2.75e-02	2.50	4.88e-03	2.50	8.63e-04

TABLE 6

Errors and convergence rates of unit normal vectors for a cosine wave test. The cosine wave is the same ($A = \frac{1}{2}, B = -\frac{1}{2}, n = 1, L = 2$) as that in [10] and it is represented by cubic splines, for which the maximum distance between two adjacent knots is $0.5h_\kappa$, $0.1h_\kappa$, $0.02h_\kappa$, and $0.01h_\kappa$ for $j = 1, 2, 3, 4$, respectively. For HFESv, the unit normal vector of the cosine wave is estimated at $\frac{1}{h_\kappa}$ points, the x -coordinates of which are evenly spaced between $x = 0$ and $x = 1$.

Method	$\mathcal{L}_\infty(h_\kappa = \frac{1}{64})$	Rate	$\mathcal{L}_\infty(h_\kappa = \frac{1}{128})$	Rate	$\mathcal{L}_\infty(h_\kappa = \frac{1}{256})$
HFESv, $j = 1$	1.31e-03	1.97	3.35e-04	2.08	7.91e-05
HFESv, $j = 2$	4.70e-05	3.99	2.96e-06	4.17	1.64e-07
HFESv, $j = 3$	5.35e-06	6.10	7.79e-08	6.29	9.96e-10
HFESv, $j = 4$	1.42e-06	8.38	4.25e-09	8.13	1.52e-11
HF2 [10, Figure 7(b)]	1.11e-03	2.04	2.69e-04	1.81	7.65e-05

times more accurate than the HF method. Furthermore, in numerically simulating multiphase flows, the cost of curvature estimation on the codimension-1 interface is dominated by that of a velocity solver of the main flow on the whole computational domain.

5.3. Cosine waves. This subsection concerns cosine waves of the form

$$(5.7) \quad y(x) = A + B \cos \frac{2n\pi x}{L}.$$

For curvature estimation, we choose the test of $A = 3, B = -1, n = 4, L = 8$ in [7, 21], which is much more challenging than the unit-circle test since values of the exact curvature contain both positive and negative numbers and have large variations near crests and troughs of the cosine wave. Errors and convergence rates listed in Table 5 clearly demonstrate the $(2j)$ th-order accuracy of the j th HFESc estimate. In addition, on the finest grid the eighth-order HFESc is thousands of times more accurate than an improved HF method [21].

In Table 5, curvature errors of HFESc based on the 1-norm for $h_\kappa = \frac{1}{20}$ are appreciably higher than that of the improved HF method. For the sixth- and the

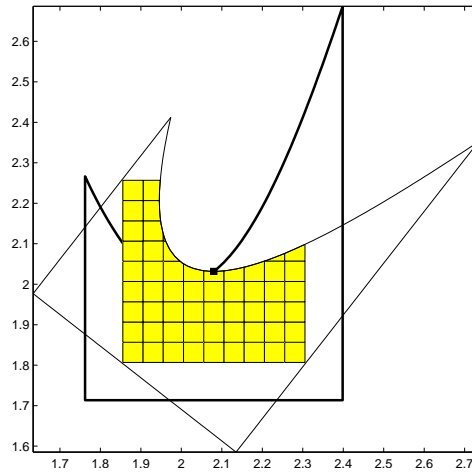


FIG. 7. A scenario of accuracy deterioration for high-order HFESc algorithms in the cosine wave test. The filled square dot represents the estimation site p , the thick closed line a Jordan curve formed from a local arc of p , and the thin closed line the rotated Jordan curve $\hat{\gamma}_r$. The shaded splines result from intersecting $\text{int}(\hat{\gamma}_r)$ to local sampling cells within a 9-by-9 grid centered at p .

eighth-order HFESc, this low accuracy is caused by the fact that after the rotation the local height function may become ill-defined within the box of size $(2j+1)h_\kappa$; see Figure 7. Fortunately, the accuracy deterioration goes away as h_κ is reduced. Also, thanks to the decoupling of h_κ from the length scale of the main flow, the large stencil width is not a disadvantage of high-order HFESc algorithms; see section 5.5 for more discussions. As for the second-order HFESc, a careful inspection of all plots similar to Figure 7 does not reveal any ill-defined height functions. So we speculate that the lower accuracy of second-order HFESc than that of the improved HF method is caused by the larger number and more even distribution of HFESc estimation sites.

To estimate unit vectors, the test of $A = \frac{1}{2}, B = -\frac{1}{2}, n = 1, L = 2$ in [10] is repeated. Errors and convergence rates are listed in Table 6, where the $(2j)$ th-order accuracy of the j th HFESv is clearly demonstrated. Once again, the eighth-order HFESv is much more accurate than another improved HF method [10], with the ratio of improving normal estimation even higher than that of curvature estimation.

5.4. Perturbation tests for an ellipse. The HFES signature in Definition 3.1 implies that the output of HFES only depends on three length scales. The first *algorithmic length scale* is the sampling size h_κ , used throughout section 3 in defining HFES. The second *perturbation length scale* of γ is ϵ_p in (4.18), as the input curve will almost always be an approximation of γ . The third *representation length scale*³ is h_L , the maximum distance between two vertices/knots on the polygon/spline that represents γ , as a discrete representation of γ always consists of a *finite* number of segments. By the Buckingham π theorem, we can characterize the behavior of HFES by two nondimensional numbers, viz., the sampling ratio and the perturbation ratio

$$(5.8) \quad r_{\text{smp}} := \frac{h_\kappa}{h_L}, \quad r_{\text{ptb}} := \frac{\epsilon_p}{h_L}.$$

³In our previous work [38, Equation 4.1] [39, Definition 3.8], h_L was called the Lagrangian length-scale of an interface.

In this subsection, the influences of the above two ratios upon the accuracy of curvature estimation are studied by perturbing an ellipse of the form

$$(5.9) \quad \mathbf{r}_E(\varphi) = (\cos \varphi, 0.6 \sin \varphi).$$

Steps of the perturbation test are as follows:

- select a number of angles $\varphi_i \in [0, 2\pi)$ so that the corresponding points calculated by $\mathbf{r}_E(\varphi_i)$ in (5.9) are roughly evenly spaced and the distance between any two adjacent points does not exceed h_L ;
- fit a cubic spline through these points and refer to it as the *smooth curve*;
- perturb knots of the smooth curve by random vectors of uniform distribution with the maximum vector length as $r_{\text{ptb}} h_L$;
- fit another cubic spline through the perturbed knots and refer to it as the *perturbed curve*;
- calculate the fourth-order HFESc estimates of the curvature at $p = \mathbf{r}_E(\frac{\pi}{12})$ for both the smooth curve and the perturbed curve with $r_{\text{ptb}} = 0.5, 10^{-2}, 10^{-4}, 10^{-8}$, and $h_\kappa = \frac{1}{4}, \frac{1}{4\sqrt{2}}, \frac{1}{8}, \dots, \frac{1}{2} h_L$.

In Figure 8, a perturbed curve of the ellipse (5.9) is shown in subplot (a), and in subplot (b) it is compared to the smooth curve within a local neighborhood of the estimation site p . Note that the deviation of the perturbed curve from the smooth curve depends on the magnitude of r_{ptb} .

We define the *algorithmic error* as the absolute difference between the exact curvature and its estimate from the smooth curve. In comparison, the *perturbation error* is the absolute difference between the two curvature estimated from the smooth curve and the perturbed curve. By the triangle inequality, the curvature estimation error of HFESc for the perturbed curve is bounded by the sum of the above two errors.

In addition to the above two errors associated with HFESc, we also define the *fit-and-differentiate errors* for another straightforward method that estimates the curvature by differentiating a C^2 cubic spline fitted through the perturbed knots. Because of the arc-length parameterization, the fitted spline $\gamma_s(s) = (x(s), y(s))$ has unit-speed and by (2.3) the magnitude of $(x''(s), y''(s))$ is an estimate of the unsigned curvature.

Values of the above three types of errors are shown in subplots (c)–(f) of Figure 8, which lead to observations as follows:

- (PTB-1) For fixed h_L and r_{ptb} , there exists a critical length scale $h_{c,j}^*$ of HFESc such that the perturbation error and the algorithmic error respectively dominates in the ranges of $h_\kappa < h_{c,j}^*$ and $h_\kappa > h_{c,j}^*$.
- (PTB-2) As r_{smp} decreases, $h_{c,j}^*$ moves toward h_L .
- (PTB-3) The j th HFESc error of curvature estimation decreases with a convergence rate of $2j$ in the range of $h_\kappa > h_{c,j}^*$. In comparison, the error increases as h further decreases in the range of $h_\kappa < h_{c,j}^*$. The occasional non-monotonicity is probably caused by the randomness of input perturbations.
- (PTB-4) Algorithmic errors increase as h_κ is further reduced in the range of $r_{\text{smp}} < 1$.
- (PTB-5) The best attainable accuracy improves as r_{ptb} is reduced.
- (PTB-6) It follows from (PTB-2), (PTB-3), and (PTB-4) that one should choose the sampling size $h_\kappa \approx h_{c,j}^*$ to achieve the best attainable accuracy.

These observations confirm the perturbation analysis in sections 4.3 and 4.4.

In computer imaging, h_L is the width of a pixel and ϵ_p could be as large as $0.5h_L$. Hence the value of r_{ptb} is typically 0.5. Then (PTB-5) explains the low accuracy of curvature estimation for digital curves in computer imaging: the perturbation ratio

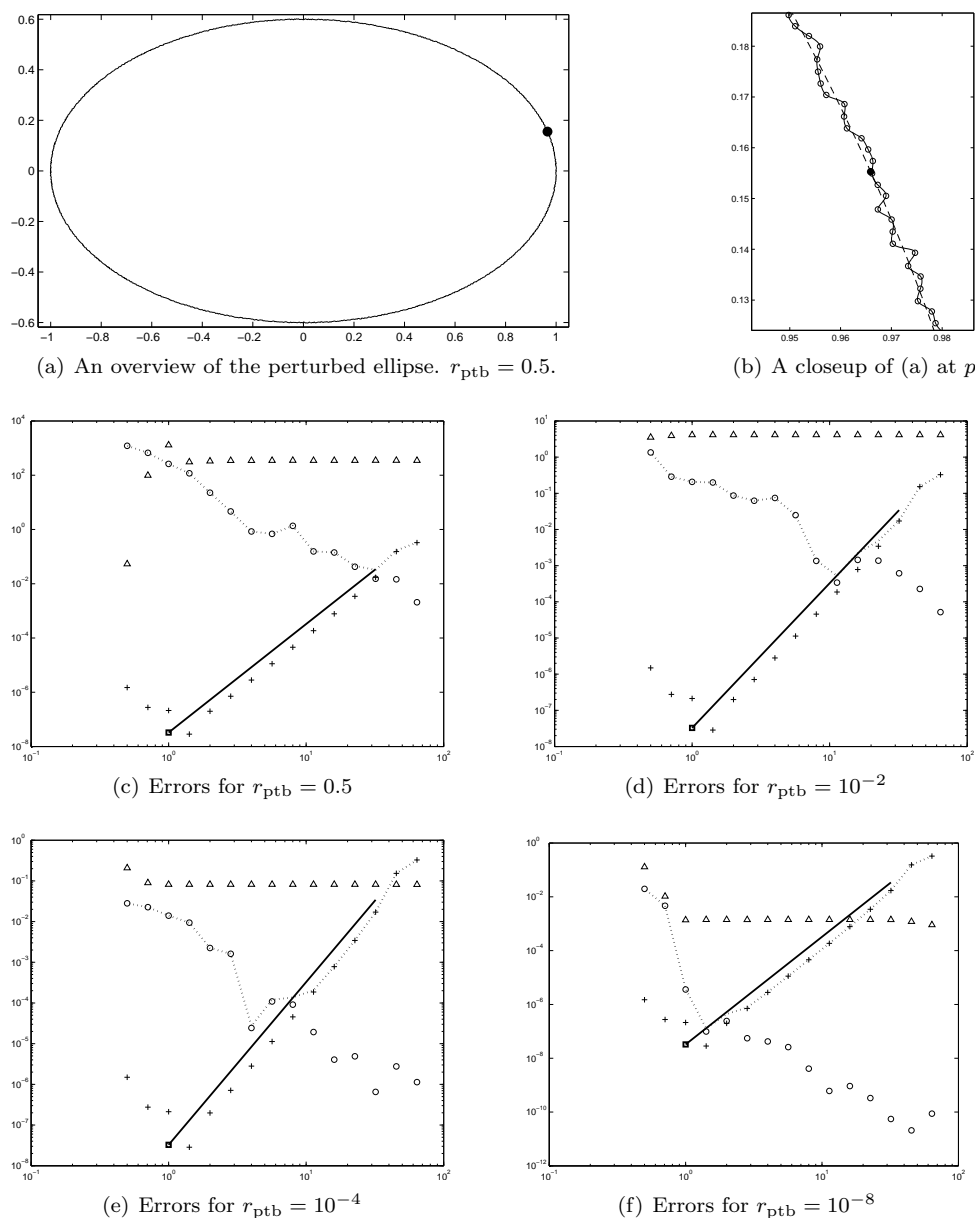


FIG. 8. Comparing the sensitivity of the fourth-order HFESc to small-scale perturbations with that of a straightforward curvature estimation method, which fits a cubic spline through the perturbed knots and differentiates the spline according to (2.3) to obtain the estimate. In subplots (a) and (b), the solid dot represents the site of estimation $p = \mathbf{r}_E(\frac{\pi}{12})$. Subplot (b) is a zoom-in of the local neighborhood of p : the dashed line and the solid line respectively represent the smooth and perturbed cubic splines, with the open circles denoting knots of the perturbed cubic spline. In subplots (c)–(f), the abscissa is r_{smp} as defined in (5.8) and the ordinate the magnitude of errors: open circles denote perturbation errors of HFESc, crosses algorithmic errors of HFESc, and triangles fit-and-differentiate errors of the straightforward method. The upper bound of HFESc curvature estimation error is represented by a solid line segment, at the end of which the x-coordinate of the square symbol denotes $r_{\text{smp}} = 1$, i.e., $h_{\kappa} = h_L$. Although subplots (c)–(f) are generated using $h_L = \frac{1}{256}$ and $j = 2$, other values of $h_L \ll 1$ and $j = 1, 3, 4$ yield qualitatively the same plots.

is simply too large to obtain accurate results, as shown in Figure 8(c). Therefore, further accuracy improvements in this field should be based on the reduction of h_L and/or r_{ptb} instead of developing new methods with the same image resolutions. After all, to extract accurate curvature from a curve, its discrete representation must carry the information at a sufficiently small length scale. This viewpoint agrees with the opinions of some previous researchers [34, 17].

In comparison to the straightforward method of spline fitting and differentiation, HFESc is less sensitive to input perturbations in that (i) its best attainable accuracy for $j = 2$ is better than that of the straightforward method by about four orders of magnitude; this improvement ratio is even greater for $j = 3, 4$; and (ii) for fixed h_L and r_{ptb} , the straightforward method does not yield improved curvature estimates when the sampling size is reduced. As discussed in section 4.3, this advantage stems from the fact that high-frequency modes corresponding to small-scale perturbations tend to be damped by the HF formulation.

5.5. Vortex-shear tests. In this test we couple HFES to the (cubic) iPAM method [38, 39, 35] to demonstrate that the high-order accuracy of HFES can indeed be realized for practical interface tracking problems. We also show how to use formulas in section 4.4 to efficiently obtain the best attainable accuracy of curvature estimation.

In the unit box $[0, 1]^2$, a transient velocity field given by the stream function

$$(5.10) \quad \psi(x, y) = -\frac{1}{\pi} \sin^2(\pi x) \sin^2(\pi y) \cos\left(\frac{\pi t}{T}\right)$$

is imposed on a circular disk, which is initially centered at $(0.5, 0.75)$ and has its radius as $R = 0.15$. During the first half time period, the disk undergoes substantial deformation; see [39, Figure 6.4(b)] for a result of the iPAM method at $t = \frac{T}{2}$ for the test of $T = 2$. During the second half time period, the velocity field is reversed by the cosinusoidal temporal factor so that the exact solution at $t = T$ coincides with the initial condition.

5.5.1. Steps to obtain the best attainable accuracy from results of an interface tracking method. In terms of interface representation, an iPAM method is *linear/cubic* if interface markers are connected by linear segments/cubic splines. There are two length scales in an iPAM method: the representation length scale h_L defined in the opening paragraph of section 5.4 and the Eulerian grid size h for resolving the main flow. An iPAM method achieves high-order accuracy by enforcing that distances between adjacent markers be in the range of $[r_{\text{tiny}}h_L, h_L]$, where $h_L = r_h h^\alpha$. For $\alpha = 2$, the linear iPAM method is analytically shown to be fourth-order accurate [39, section 5.2]. It is also shown numerically in [39, 35] that, by setting $\alpha = 1, \frac{3}{2}, 2$, a cubic iPAM method can be respectively fourth-, sixth-, and eighth-order accurate. Table 7 contains some results obtained in [35] by a cubic iPAM method. On the finest grid in test (C) the final circular disk is resolved to machine precision!

Results of test cases (A), (B), and (C) are then passed as perturbed input into HFES to estimate curvature and unit normal vectors. An HFES algorithm is chosen so that its convergence rate is the same as that of the cubic iPAM method for generating the input. To most efficiently obtain the best attainable accuracy offered by the perturbed input, we utilize the formulas derived in section 4.4 to select the sampling size h_κ . The steps are as follows:

- (SSC-1) Since the exact interface is a circle, we calculate the derivatives $H^{(2j+2)}(0)$ from (4.15), yielding the third and fourth columns of Table 8.

TABLE 7

Interface tracking errors and convergence rates of a cubic iPAM method with $r_{\text{tiny}} = 0.01$ for the vortex shear test of $T = 2$. The results here are taken from [35].

Test	$h = \frac{1}{16}$	rate	$h = \frac{1}{32}$	rate	$h = \frac{1}{64}$
(A) $h_L = 0.1h$	3.53e-06	4.98	1.12e-07	4.99	3.52e-09
(B) $h_L = h^{\frac{3}{2}}$	3.50e-08	6.51	3.84e-10	6.56	4.08e-12
(C) $h_L = h^2$	4.93e-11	7.87	2.10e-13	9.89	2.22e-16

TABLE 8

The estimation of critical sampling sizes by formulas in Table 2 and results of the iPAM method with $h = \frac{1}{64}$ in Table 7. The purpose of these calculations is to select “ideal” sampling sizes (in terms of h) for curvature estimation by HFESc. Note that the values of $H^{(2j+2)}(0)$ in Table 1 are for the unit circle, whereas those of $H^{(2j+2)}(0)$ here are for a circle with $R = 0.15$.

Test	j	$H^{(2j+2)}$	$(H^{(2j+2)})^{\frac{1}{j+1}}$	$\epsilon_p = \frac{E_1}{2\pi R}$	$h_{c,j}^*$	$\frac{h_{c,j}^*}{h}$	$E_{c,j}^*$
(A)	2	5.93e+05	8.40e+01	3.73e-09	9.97e-03	0.638	3.38e-04
(B)	3	9.22e+08	1.74e+02	4.33e-12	6.56e-03	0.420	9.73e-07
(C)	4	2.58e+12	3.04e+02	2.36e-16	3.53e-03	0.226	1.92e-10

(SSC-2) The perturbation length scale is estimated as $\epsilon_p \approx E_1/\|\partial\mathcal{M}(T)\|$, where E_1 is the volume of the symmetric difference of the exact and computed solutions shown in the last column of Table 7, and $\|\partial\mathcal{M}(T)\|$ is the length of the interface at the final time. See the fifth column of Table 8.

(SSC-3) Critical sampling sizes are calculated by formulas in the second column of Table 2, yielding the sixth and the seventh columns of Table 8. Values of the corresponding best attainable accuracy on uniform grids are also listed in the last column of Table 8.

(SSC-4) The analysis in section 4.4 and numerical experiments in section 5.4 suggest $h_\kappa > h_{c,j}^*$, hence the sampling size should be slightly greater than $h_{c,j}^*$.

According to (SSC-4), we choose $h_\kappa = 0.65h, 0.45h, 0.25h$ for tests (F), (G), and (H) in which curvature and unit normal are estimated from results of tests (A), (B), and (C), respectively. In Table 9, the fourth-, sixth-, and eighth-order accuracy of both HFESc and HFESv are clearly demonstrated, indicating that *an HFES algorithm works well with a cubic iPAM method*.

With selected sampling sizes close to the critical sampling sizes in Table 8, we also expect that curvature estimation errors on the finest uniform grid will be very close to the best attainable accuracy. Actual results shown in Table 10, however, vary from test to test. For test (F), the “theoretical” best attainable accuracy is about 68 times greater than the “actual” best attainable accuracy, indicating that the formulas derived in section 4.4 may be too conservative. This is not a surprise, though. After all, one prominent advantage of splines in curve fitting is its capability of suppressing oscillations. Hence the worst case accounted for in (4.20) seldom takes place when distances between adjacent knots are relatively large in terms of the sampling size h_κ . This is indeed the case with test (F) since their asymptotic ratio is $\frac{h_L}{h_\kappa} = O(1)$. However, for tests (G) and (H), where the input curves are results of tests (B) and (C), the ratio $\frac{h_L}{h_\kappa}$ is respectively $O(h^{\frac{1}{2}})$ and $O(h)$ and is asymptotically smaller than that of test (F). Hence it is much more likely that the worst case in (4.20) will be frequently realized in tests (G) and (H). Consequently, the difference between the “theoretical” and “actual” best attainable accuracy for tests (G) and (H) is much smaller than that for test (F). In particular, the difference is only 13% for test (H).

TABLE 9

Errors and convergence rates of HFES for the vortex shear test of $T = 2$. The input into tests (F), (G), and (H) is the final results of tests (A), (B), and (C), respectively.

Test	$h = \frac{1}{16}$	Rate	$h = \frac{1}{32}$	Rate	$h = \frac{1}{64}$
Curvature errors based on the 1-norm					
(F) HFESc: $j = 2, h_\kappa = 0.65h$	9.58e-02	4.53	4.15e-03	4.08	2.46e-04
(G) HFESc: $j = 3, h_\kappa = 0.45h$	6.05e-03	6.86	5.22e-05	5.99	8.21e-07
(H) HFESc: $j = 4, h_\kappa = 0.25h$	1.52e-05	8.32	4.76e-08	7.78	2.17e-10
Unit normal errors based on the 1-norm					
(F) HFESv: $j = 2, h_\kappa = 0.65h$	8.31e-02	4.74	3.12e-03	3.88	2.12e-04
(G) HFESv: $j = 3, h_\kappa = 0.45h$	8.14e-02	7.49	4.52e-04	6.60	4.67e-06
(H) HFESv: $j = 4, h_\kappa = 0.25h$	5.90e-03	10.63	3.72e-06	8.85	8.07e-09

TABLE 10

Curvature errors and corresponding sampling sizes in estimating the best attainable accuracy on uniform grids. The first and fourth columns, i.e., the “theoretical” best attainable accuracy and corresponding sampling sizes, are taken from Table 8. The second and fifth columns, i.e., the “approximate” best attainable accuracy and corresponding sampling sizes, are taken from Table 9. The third and sixth columns, the “actual” best attainable accuracy and corresponding sampling sizes, are obtained as follows. HFESc is repeated for the sampling sizes $h_\kappa \pm 0.02jh$, $j \in \mathbb{N}$, until a local infimum of curvature estimation error is reached. Then the infimum and its corresponding sampling size are taken to be $E_{c,j}^\Delta$ and $h_{c,j}^\Delta$, respectively.

Test	$2j$	h_L	$E_{c,j}^*$	$\mathcal{L}_1(E_\kappa)$	$E_{c,j}^\Delta$	$h_{c,j}^*$	h	$h_{c,j}^\Delta$
(F)	4	$0.1h$	3.38e-04	2.46e-04	4.96e-06	$0.638h$	$0.65h$	$0.21h$
(G)	6	$h^{\frac{3}{2}}$	9.73e-07	8.21e-07	5.21e-07	$0.420h$	$0.45h$	$0.38h$
(H)	8	h^2	1.92e-10	2.17e-10	2.17e-10	$0.226h$	$0.25h$	$0.25h$

Leading truncation errors of HFES contain high-order derivatives of the local height function, and the careful reader may have already noticed in the third column of Table 8 that $|H^{(2j+2)}|$ grows very fast as j increases. However, by the analysis in section 4.4, the best attainable accuracy on uniform grids is proportional not to $H^{(2j+2)}$ but to $(H^{(2j+2)})^{\frac{1}{j+1}}$, the value of which grows rather slowly, as shown by the fourth column of Table 8.

5.5.2. Factors of accuracy improvement of HFES over previous HF methods. Both section 5.5.1 and section 5.2 concern a circle. However, the circle tested in section 5.5.1 has a diameter of only $\frac{3}{20}$, much smaller than 1 of the unit circle in section 5.2. Hence it would be informative (and to some degree complementary to section 5.2) to compare results of HFES in section 5.5.1 to those of previous HF methods. Table 11 contains this comparison.

For results on $h = \frac{1}{64}$, the eighth-order HFESc algorithm is more accurate than the fourth-order HF method by a factor of $\frac{1.62 \times 10^{-2}}{2.17 \times 10^{-10}} \approx 7.47 \times 10^7$! Since the input into these two methods is the same, this drastic difference in accuracy must be caused by the following three factors of accuracy improvement (FAIs):

- (FAI-1) the flexibility of choosing $h_\kappa < h$ to achieve the best attainable accuracy,
- (FAI-2) a smaller truncation error of a higher-order formula,
- (FAI-3) reduction of the leading truncation error via rotating the local arc.

Pairwise comparisons of test results in Table 9 show contributions from all three FAIs. First, (FAI-1) contributed a factor of $\frac{1.62 \times 10^{-2}}{4.61 \times 10^{-5}} \approx 351$ since tests (K) and (L) differ only in their sampling sizes. In other words, if the fourth-order HF method could use a sampling size smaller than the Eulerian grid size, it would have been 351

TABLE 11

A comparison of HFES to previous HF methods in estimating curvature for the vortex shear test of $T = 2$. Tests (L) and (N) are typical cases of fourth-order and second-order HF methods coupled to VOF methods without adaptive mesh refinement; results of these two tests are obtained by our implementation. As mentioned in section 3.3, the second-order HF method [13, 29] and the fourth-order HF method [30, 4] are essentially the same as HFESv with $j = 1$ and $j = 2$, respectively. Hence tests (K) and (L) differ only in their sampling sizes, as do tests (M) and (N).

Test	$h = \frac{1}{32}$	Rate	$h = \frac{1}{64}$
(H) 8th-order HFESc, $h_\kappa = 0.25h$	4.76e-08	7.78	2.17e-10
(J) 8th-order HFESv, $h_\kappa = 0.25h$	6.69e-05	8.94	1.36e-07
(K) 4th-order HFESv, $h_\kappa = 0.25h$	8.07e-04	4.13	4.61e-05
(L) 4th-order HF method [30, 4], $h_\kappa = h$	4.54e-01	4.81	1.62e-02
(M) 2nd-order HFESv, $h_\kappa = 0.25h$	1.71e-02	2.00	4.29e-03
(N) 2nd-order HF method [13, 29], $h_\kappa = h$	3.31e-01	2.23	7.06e-02

times more accurate. Second, (FAI-2) contributed a factor of $\frac{4.61 \times 10^{-5}}{1.36 \times 10^{-7}} \approx 339$ since the only difference between tests (K) and (J) is the order of accuracy. Last, (FAI-3) contributed a factor of $\frac{1.36 \times 10^{-7}}{2.17 \times 10^{-10}} \approx 627$ since the only difference between tests (J) and (H) is the rotation of local arcs. Similar to discussions in section 5.2, the above simple calculations show that rotation of local arcs made the biggest contribution to accuracy improvement. In addition, the contribution from the flexibility of choosing $h_\kappa < h$ is comparable to that of the high-order formula.

As for unit normal estimation on the grid of $h = \frac{1}{64}$, the eighth-order HFES algorithm is more accurate than the fourth-order HF method by a factor of 1.54×10^5 , out of which (FAI-1) contributed a factor of 304 and (FAI-2) a factor of 506. The smaller improvement ratio than that of curvature estimation is probably due to the irrelevance of (FAI-3) and the fact that the selected sampling sizes are not optimized for unit normal estimation. In other words, unit normal errors of HFESv could have been smaller if formulas in the third and fourth columns of Table 2 had been used in the steps (SSC-1) through (SSC-4) to estimate a different set of critical sampling sizes.

It would be very difficult for VOF-based methods to realize all of (FAI-1) through (FAI-3). Results of tests (C) and (H) in Tables 7 and 9 indicate that, with double-precision floating point numbers, the best attainable accuracy of the eighth-order HFESc is about 10 decimal digits, whereas the best we can hope for by the eighth-order HF method is about six decimal digits of accuracy. Hence the fourth-order HF formula can never be as accurate as the eighth-order HFESc. However, we emphasize that the high accuracy of HFESc is based on that of the iPAM method and that the much better accuracy of HFESc+iPAM over HF+VOF can be realized only when the underlying velocity field is sufficiently accurate.

5.5.3. The different asymptotic regimes of shape analysis in computer imaging and numerical simulation in multiphase flows. In comparison to the typical input with $r_{\text{ptb}} \approx 0.5$ in computer imaging (see the discussion in section 5.4), the input generated by the iPAM method satisfies

$$(5.11) \quad r_{\text{ptb}} = O\left(\frac{E_1}{h_L}\right) = O\left(\frac{h^\beta}{h^\alpha}\right) = O(h^{\beta-\alpha}),$$

where α is the power coefficient in the relation $h_L = r_h h^\alpha$ enforced by the iPAM method and β its convergence rate. The fact of $\beta \geq \alpha + 1$ for all iPAM methods implies that $r_{\text{ptb}} \rightarrow 0$ as $h \rightarrow 0$. Hence the best attainable accuracy decreases as h

is reduced, as demonstrated in Figure 8 (c)–(f). This explains why we were able to obtain the $(2j)$ th convergence rates of the j th HFES algorithm from results of the iPAM method.

6. Conclusions. Motivated by a list of open questions, we have developed the HFES method for estimating the curvature and unit vectors of planar curves. Compared to previous HF methods, HFES has distinguishing features such as the following:

- (a) High convergence rates: formulas of the j th HFES estimates are shown to be $(2j)$ th-order accurate for $j = 1, 2, 3, 4$.
- (b) Rigorousness: HFES is based on a solid theoretical ground, which unifies all HFES formulas and admits further generalization to even higher convergence rates; see the short MATLAB program in Figure 4.
- (c) Generality: HFES is applicable to both shape analysis in computer imaging and numerical simulation in multiphase flows.
- (d) Explicit spline representation: this unleashes the representational power of cubic splines, the accuracy of which is preserved by splinegon clipping.
- (e) Freedom: the curvature of any point on the input curve can be directly estimated with no interpolation.
- (f) Flexibility: the sampling size h_κ of HFES is completely decoupled both from the grid size h for resolving the main flow and from the Lagrangian length scale h_L for representing the curve. One can set $h_\kappa < h$ to efficiently achieve the best attainable accuracy on uniform grids as shown in section 5.5.
- (g) User-friendliness: the signs of HFES estimates can be chosen intuitively by selecting orientations of input Jordan curves according to the application at hand, without knowing any details of the algorithm. Also, the signs immediately indicate relative positions of the two phases and the local shape of the interface.
- (h) Rotation of local arcs: the corresponding reduction of the leading truncation error grows with the increase of order of accuracy; improvement ratios over a thousand are observed in numerical experiments.

The high accuracy of HFES is due to (a), (d), (f), and (h). In using VOF methods to simulate multiphase flows, however, it is difficult to realize the same level of accuracy of HFES+iPAM as demonstrated in this work because neither the implicit volume fractions nor the explicit piecewise function preserves enough information of the interface. Hence the accuracy improvement should be ascribed to HFES+iPAM over HF+VOF, rather than HFES alone over previous HF methods. On the other hand, the formal description of the HF approach and its numerical analysis might still be useful for further developing curvature estimation algorithms that are intended to be coupled with VOF methods.

Many real-world multiphase applications entail numerically solving the main flow to produce a velocity field for interface tracking. To realize the accuracy advantage of HFES+iPAM, such a main flow solver will also have to be accurate enough. For this purpose, we are currently in the process of assembling HFES, the iPAM method, and a family of fourth-order finite-volume methods [40, 36] into a high-order computational framework for simulating multiphase flows with moving interfaces.

As another research prospect, HFES can be further augmented to estimate the curvature and unit normal of a regular surface embedded in the three-dimensional Euclidean space.

Acknowledgment. The author is grateful to one anonymous referee, whose comments led to an improvement on the quality of this paper.

REFERENCES

- [1] H. ASADA AND M. BRADY, *The curvature primal sketch*, IEEE Trans. Pattern Anal. Machine Intelligence, 8 (1986), pp. 2–14.
- [2] F. ATTNEAVE, *Some informational aspects of visual perception*, Psychological Rev., 61 (1954), pp. 183–193.
- [3] H. L. BEUS AND S. S. H. TIU, *An improved corner detection algorithm based on chain-coded plane curves*, Pattern Recognit., 20 (1987), pp. 291–296.
- [4] G. BORNIA, A. CERVONE, S. MANSERVISI, R. SCARDOVELLI, AND S. ZALESKI, *On the properties and limitations of the height function method in two-dimensional Cartesian geometry*, J. Comput. Phys., 230 (2011), pp. 851–862.
- [5] E. CALABI, P. J. OLVER, C. SHAKIBAN, A. TANNENBAUM, AND S. HAKER, *Differential and numerically invariant signature curves applied to object recognition*, Int. J. Comput. Vis., 26 (1998), pp. 107–135, doi:10.1023/A:1007992709392.
- [6] D. COEURJOLLY, S. MIGUET, AND L. TOUGNE, *Discrete curvature based on osculation circle estimation*, in Proceedings of the International Workshop Visual Form, Lecture Notes in Comput. Sci. 2059, Springer, Berlin, 2001, pp. 300–312.
- [7] S. J. CUMMINS, M. M. FRANCOIS, AND D. B. KOTHE, *Estimating curvature from volume fractions*, Comput. Struct., 83 (2005), pp. 425–434.
- [8] L. DA FONA COSTA AND R. M. CESAR, JR., *Shape Classification and Analysis: Theory and Practice*, 2nd ed., Image Processing Series, CRC Press, Boca Raton, FL, 2009.
- [9] F. DENNER, D. R. VAN DER HEUL, G. T. OUD, M. M. VILLAR, A. D. S. NETO, AND B. G. M. VAN WACHEM, *Comparative study of mass-conserving interface capturing frameworks for two-phase flows with surface tension*, Int. J. Multiphase Flow, 61 (2014), pp. 37–47.
- [10] P. A. FERDOWSI AND M. BUSSMANN, *Second-order accurate normals from height functions*, J. Comput. Phys., 227 (2008), pp. 9293–9302.
- [11] M. M. FRANCOIS AND B. K. SWARTZ, *Interface curvature via volume fractions, heights and mean values on nonuniform rectangular grids*, J. Comput. Phys., 229 (2010), pp. 527–540.
- [12] H. FREEMAN AND L. S. DAVIS, *A corner-finding algorithm for chain-coded curves*, IEEE Trans. Comput., 26 (1977), pp. 297–303.
- [13] J. HELMSEN, P. COLELLA, AND E. G. PUCKETT, *Non-Convex Profile Evolution in Two Dimensions Using Volume of Fluids*, Tech. report LBNL-40693, Lawrence Berkeley National Laboratory, 1997.
- [14] S. HERMANN AND R. KLETTE, *Multigrid analysis of curvature estimators*, in Proceedings of Image Vision Computing, Massey University, New Zealand, 2003, pp. 108–112.
- [15] L. KITCHEN AND A. ROSENFELD, *Gray-level corner detection*, Pattern Recognition Lett., 1 (1982), pp. 95–102.
- [16] J. J. KOENDERINK AND W. RICHARDS, *Two-dimensional curvature operators*, J. Opt. Soc. Amer. A, 5 (1988), pp. 1136–1141.
- [17] V. KOVALEVSKY, *Curvature in digital 2D images*, Internat. J. Pattern Recognit. Artif. Intell., 15 (2001), pp. 1183–1200.
- [18] B. LAFAURIE, C. NARDONE, R. SCARDOVELLI, S. ZALESKI, AND G. ZANETTI, *Modeling merging and fragmentation in multiphase flows with SURFER*, J. Comput. Phys., 113 (1994).
- [19] S. K. LELE, *Compact finite difference schemes with spectral-like resolutions*, J. Comput. Phys., 103 (1992), pp. 16–42.
- [20] P. LIOVIC, M. FRANCOIS, M. RUDMAN, AND R. MANASSEH, *Efficient simulation of surface tension-dominated flows through enhanced interface geometry interrogation*, J. Comput. Phys., 229 (2010), pp. 7520–7544.
- [21] J. LÓPEZ AND J. HERNÁNDEZ, *On reducing interface curvature computation errors in the height function technique*, J. Comput. Phys., 229 (2010), pp. 4885–4868.
- [22] J. LÓPEZ, C. ZANZI, P. GÓMEZ, R. ZAMORA, F. FAURA, AND J. HERNÁNDEZ, *An improved height function technique for computing interface curvature from volume fractions*, Comput. Methods Appl. Mech. Engrg., 198 (2009), pp. 2555–2564.
- [23] M. MARJI, *On the Detection of Dominant Points on Digital Planar Curves*, Ph.D. thesis, Wayne State University, Detroit, MI, 2003.
- [24] F. MOKHTARIAN AND A. MACKWORTH, *Scale-based description and recognition of digital curves and two-dimensional shapes*, IEEE Trans. Pattern Anal. Mach. Intell., 8 (1986), pp. 34–43.
- [25] M. OWKES AND O. DESJARDINS, *A mesh decoupled height function method for computing interface curvature*, J. Comput. Phys., 281 (2015), pp. 285–300.
- [26] S. POPINET, *An accurate adaptive solver for surface-tension-driven interfacial flows*, J. Comput. Phys., 228 (2009), pp. 5838–5866.
- [27] A. PRESSLEY, *Elementary Differential Geometry*, 2nd ed., Springer, London, 2010.

- [28] Y. RENARDY AND M. RENARDY, *PROST: A parabolic reconstruction of surface tension for the volume-of-fluid method*, J. Comput. Phys., 183 (2002), pp. 400–421.
- [29] M. SUSSMAN, *A second order coupled level set and volume-of-fluid method for computing growth and collapse of vapor bubbles*, J. Comput. Phys., 187 (2003), pp. 110–136.
- [30] M. SUSSMAN AND M. OHTA, *High-order techniques for calculating surface tension forces*, Internat. Ser. Numer. Math., 154 (2006), pp. 425–434.
- [31] M. SUSSMAN AND M. OHTA, *Improvements for calculating two-phase bubble and drop motion using an adaptive sharp interface method*, Fluid Dyn. Mater. Proc., 3 (2007), pp. 21–36.
- [32] M. W. WILLIAMS, *Numerical Methods for Tracking Interfaces with Surface Tension in 3D Mold Filling Processes*, Ph.D. thesis, University of California, Davis, 2000.
- [33] M. W. WILLIAMS, D. B. KOTHE, AND E. G. PUCKETT, *Accuracy and convergence of continuum surface-tension models*, in Fluid Dynamics at Interfaces, R. N. W. Shyy, ed., Cambridge University Press, Cambridge, UK, 1998, pp. 294–305.
- [34] M. WORRING AND A. W. M. SMEULDERS, *Digital curvature estimations*, CVGIP Image Understanding, 58 (1993), pp. 366–382.
- [35] Q. ZHANG, *The cubic iPAM method for fourth- and higher-order interface tracking in two dimensions for an arbitrary number of materials*, submitted.
- [36] Q. ZHANG, *GePUP: Generic projection and unconstrained PPE for fourth-order solutions of the incompressible Navier-Stokes equations with no-slip boundary conditions*, J. Sci. Comput., 67 (2016), pp. 1134–1180.
- [37] Q. ZHANG, *Boolean algebra on physically meaningful regions in the plane*, submitted.
- [38] Q. ZHANG AND A. FOGELSON, *Fourth-order interface tracking in two dimensions via an improved polygonal area mapping method*, SIAM J. Sci. Comput., 36 (2014), pp. A2369–A2400.
- [39] Q. ZHANG AND A. FOGELSON, *MARS: An analytic framework of interface tracking via mapping and adjusting regular semialgebraic sets*, SIAM J. Numer. Anal., 54 (2016), pp. 530–560.
- [40] Q. ZHANG, H. JOHANSEN, AND P. COLELLA, *A fourth-order accurate finite-volume method with structured adaptive mesh refinement for solving the advection-diffusion equation*, SIAM J. Sci. Comput., 34 (2012), pp. B179–B201.